Tectonophysics 847 (2023) 229689

Contents lists available at ScienceDirect

Tectonophysics

journal homepage: www.elsevier.com/locate/tecto

Modeling frictional precursory phenomena using a wear-based rate- and state-dependent friction model in the laboratory

P.A. Selvadurai [a,*], P. Galvez [b], P.M. Mai [b], S.D. Glaser [c]

[a] Swiss Seismological Service, ETH Zurich, Zurich, Switzerland
[b] King Abdullah University of Science and Technology, Thuwal, Saudi Arabia
[c] Civil and Environmental Engineering, University of California, Berkeley, CA, USA

ARTICLE INFO

Keywords:
Earthquake sequences
Rate- and state-dependent friction
Numerical simulations
Hierarchical asperities
Worn interface

ABSTRACT

We examine numerical models that employ the rate-and-state frictional (RSF) framework to investigate earthquake sequences using laboratory driven descriptions of heterogeneous frictional properties. Using previously obtained experimental measurement of roughness, we observed that wear produced a bimodal Gaussian distribution of surface heights, which we hypothesized produced spatial heterogeneity of the critical slip distance D_c. In this numerical study, the fault surface was binarized into discrete smooth or rough sections, producing a *barcode style* version of frictional heterogeneity. The fault was predominantly rough except for two dominant asperities ($A1$ and $A2$) representative of larger polished sections. We simulated the resistive effect of increasing the fracture energy (toughness) of the rough barriers while maintaining constant properties of the embedded brittle/smooth asperities. Our numerical simulations generated burst-like seismic events and aseismic transients throughout the interseismic phase. At the late interseismic phase, bursts of seismicity (foreshocks) interacted with the accelerating preslip region at the transition to the preseismic (nucleation) phase. At lower levels of toughness heterogeneity, the slip rate increase was roughly inversely proportional to the time-to-failure t_f for larger events. As fault toughness was increased, the dominant asperities initiated nucleation and thus force deviations of the fault from the smooth $1/t_f$ acceleration observed for the homogeneous case, producing a rate-dependent cascade response. The calculations were validated by comparing two independently measured metrics from the experiments: (1) The expansion rate of slow ruptures during the interseismic and preslip phase and (2) the scalar seismic moment and source dimensions. While our study does not address the scaling problem, these results help to understand laboratory experiments that investigate transition to the preseismic (nucleation) phase during complex earthquake sequences.

1. Introduction

Seismologic observations have captured a growing diversity in slip behavior along natural faults suggesting that coupling of faults and the ability to resist frictional breakdown is spatially heterogeneous. Heterogeneity in frictional properties is necessary to explain observations, such as precursory seismicity, that has been detected in regions that also host the steady growth of a preslip region and subsequent mainshock (Kato et al., 2012, 2016; Obara and Kato, 2016). It is not currently possible to predict when and where precursory seismicity will occur and whether it carries information on the timing and size of the impending mainshock (Brodsky and Lay, 2014).

One model proposed to explain certain aspects of seismicity and the slow accumulation of fault slip is the *preslip model*, which predicts a region of increased slow slip that grows outwards to a critical size where it nucleates and the mainshock ensues (Ohnaka and Yamashita, 1989; Ohnaka, 1992, 1993). Recent improvements in geodetic measurements have been able to lower the detection threshold of slow transients, which are in some cases inferred to be the nucleation phase over long time scales (months to years) and length scales (kms) (e.g., Roeloffs, 2006; Wang and Bilek, 2014). In certain cases, precursory seismicity in the form of foreshocks have been observed days to months prior to the mainshock (Dodge et al., 1995; Bouchon et al., 2011; Bürgmann, 2014). In the preslip model, foreshocks are triggered by aseismic loading of patches that are due to frictional heterogeneity within the preparatory region. However, the mainshock onset, i.e. the transition to the large

* Corresponding author.
E-mail address: paul.selvadurai@sed.ethz.ch (P.A. Selvadurai).

https://doi.org/10.1016/j.tecto.2022.229689
Received 28 February 2022; Received in revised form 8 October 2022; Accepted 11 December 2022
Available online 28 December 2022

scale nucleation phase, is governed by the overall size of the growing preslip region and not associated with triggering by the foreshock.

A competing end-member model is the *cascading model*, where studies of the initial onset of seismic rupture suggest that asperities exist at many spatial scales, and that the triggering of a cascading-style failure mechanism might stem from failure of a smaller section (e.g. Ellsworth and Beroza, 1995; Beroza and Ellsworth, 1996; Ellsworth and Bulut, 2018). These are characteristic of a stochastic model (Gomberg, 2018) in which the timing and size seismicity are independent of the initiating perturbation. This differs from the deterministic preslip model, where the propagating slow-slip front triggers failure of strong patches as they are loaded. While it is unclear if all mainshocks are always preceded by foreshocks (Brodsky and Lay, 2014; Mignan, 2014; Seif et al., 2018) they are currently only identifiable in retrospective analysis. Recent laboratory studies have shed light into possible relationship between cascading sequences of earthquake and the overriding preparation process of larger events (Yamashita et al., 2021). With more refined models, foreshock activity may be used to constrain the current and future state of the fault, making for an improved assessment of earthquake hazard. These types of models can benefit from laboratory friction experiments.

The spatio-temporal growth of a preslip region and its transition from slow (quasi-static) to fast (dynamic) slip has been well documented in laboratory experiments (Dieterich, 1978; Okubo and Dieterich, 1984; Ohnaka and Shen, 1999; Nielsen et al., 2010; Latour et al., 2013; Fukuyama et al., 2018; Zhuo et al., 2018a; Ke et al., 2018; Xu et al., 2019; Buijze et al., 2020). Along with measuring the spatio-temporal evolution of slow premonitory slip, acoustic emission sensors have been deployed to detect localized seismicity that spontaneously emanates from sections of the fault that also hosted the preslip region (Ma et al., 2002; McLaskey and Kilgore, 2013; McLaskey and Lockner, 2014; Selvadurai and Glaser, 2015; Passelègue et al., 2017; Zhuo et al., 2018b). Analysis of the ground motions produced by laboratory seismicity using seismological models found that the moment released over their geometric sizes scaled with empirical relationships observed in natural earthquakes (McLaskey et al., 2014; Selvadurai, 2019). These observations have stimulated studies on laboratory seismicity and its connection to the growth and stability of the preslip region (McLaskey, 2019).

Laboratory foreshocks have been reported well before mainshock rupture (McLaskey and Kilgore, 2013; Selvadurai and Glaser, 2015). However, contrasting observations have been reported, in that the foreshocks follow the runaway cascading model or a combination of both (McLaskey et al., 2014; Yamashita et al., 2021). In these tests, heterogeneity in frictional properties are related to the geometric interaction between two rough surfaces that give rise to local variations in contact conditions (e.g. Yoshioka, 1997; Schmittbuhl et al., 2006). This contact stress heterogeneity was confirmed by Selvadurai and Glaser (2017) with measurement of spatially variable normal stress determined from a pressure sensitive film placed along the interface and also visually using photometric methods (Dieterich and Kilgore, 1994; Selvadurai and Glaser, 2015). These highly stressed asperities may induce patches susceptible to localized seismicity (Selvadurai and Glaser, 2017) or potentially foreshocks if this occurs near the transition to gross fault rupture. The mechanisms and conditions that controls the occurrence of foreshocks (or other types of precursory seismicity) during the late interseismic phase of the earthquake cycle, even at laboratory scales, are still not entirely clear. While many groups have tried to answer these questions, the effect of frictional heterogeneity on a fault is not yet completely understood in relation to the asperities formed at the interface of rough surfaces: What is the effect of frictional heterogeneity on the interface behavior? How does this affect the preparatory processes?

In this study, we examine numerical models that employ the rate-and-state frictional (RSF) framework to investigate earthquake sequences using laboratory driven descriptions of heterogeneous frictional properties. Mechanisms explaining localized fast ruptures embedded within a larger slow preparatory rupture are investigated here. Our simulations are used to explain a suite of well-documented friction experiments that observed such behavior (Selvadurai and Glaser, 2015; Selvadurai and Glaser, 2017; Selvadurai et al., 2017; Selvadurai, 2019, see summary in Supplemental Section S1).

2. Background

Numerical RSF models have been successfully used to understand various aspects of earthquake cycles and fault mechanics (Dieterich, 1979; Ruina, 1983; Rice, 1993; Lapusta and Rice, 2003). The RSF model origins are phenomenological and derived from various frictional tests in the laboratory and offer a unified and robust formulation that explains the logarithmic strengthening of fault with hold time and slip-weakening behavior that is also capable of producing dynamic instability. This friction law has been widely used to study, e.g. the nucleation processes (Castellano et al., 2023; Lapusta and Rice, 2003; Rice, 1993; Rubin and Ampuero, 2005), aseismic transients (Liu and Rice, 2005; Liu and Rice, 2007; Ozawa et al., 2019; Dal Zilio et al., 2020), repeating earthquakes (Chen and Lapusta, 2009; Kato, 2003; Noda et al., 2013; Cattania and Segall, 2019), earthquake sequences (Tse and Rice, 1986; Ben-Zion and Rice, 1995; Dieterich and Richards-Dinger, 2010; Kaneko et al., 2010; Barbot et al., 2012; Shi et al., 2020; Heimisson, 2020; Ozawa and Ando, 2021; Cattania and Segall, 2021), slip instability of a fluid-infiltrated fault (Segall and Rice, 1995; Kroll et al., 2017), fault sections with complex geometric interactions (Romanet et al., 2018; Yin et al., 2022) and even glacial icequakes (Lipovsky and Dunham, 2017; Köpfli et al., 2022).

Hillers et al. (2006) studied the effect of random spatial distribution of the critical slip distance D_c on a large, potentially seismogenic asperity at depths from −5 to −14 km. They found that heterogeneity in D_c controlled the number of seismic events and fluctuations in stress level and they were able to reproduce a frequency-magnitude distribution spanning 4 orders that followed the Gutenberg-Richter law. Hillers et al. (2007) extended this work to examine the effect of end-member distributions of D_c (uniform and Gaussian) on the pattern of seismicity at the mentioned depths. Our study increases our ability to understand the effects of spatial variations in D_c that are inferred from laboratory tests.

In dry, gouge-free and unlubricated faults, D_c is related to how asperities form with respect to the surface roughness and are described by the micromechanics of multi-contact interfaces (Yoshioka and Scholz, 1989; Dieterich and Kilgore, 1994; Baumberger and Caroli, 2006). D_c has been interpreted as the displacement required to completely change the population of contact points (Dieterich, 1979) and is intrinsically linked to roughness via concepts described in the field of contact mechanics (e.g. Johnson, 1985). Since the contacts will behave collectively (unlike the single contact model by Rabinowicz (1956)) there may be at least two possible interpretations for D_c: (1) It is the distance over which the contacts existing at the moment of change in slip rate fade away and are replaced by new asperity contacts with different properties, or (2) it is the distance required for a complete replacement of the real contact "area" that existed at the moment of the step change in sliding velocity. Laboratory experiments have shown that smoother faults exhibit lower D_c than rough ones (Marone and Cox, 1994; Ohnaka and Shen, 1999). This assumption also follows micromechanical simulations governing the critical slip distance D_c for dry, gouge-free interfaces (Yoshioka and Iwasa, 1996; Yoshioka, 1997). It is being shown potentially more than one weakening mechanism can contribute to frictional dissipation in cohesive rocks (Cornelio et al., 2022) and this may also affect critical slip distance over which shear stress is reduced but this is not considered in this work. Moreover, we recognize that dissipation of energy on natural faults likely occurs on complex fault structures within a single core (see Fig. 2A in Cocco et al., 2023) but this is beyond the scope of this study. Instead, we use the previous findings that link roughness to critical slip distance via contact mechanics, to impose heterogeneous distribution of

frictional properties on a worn planar interface.

Fig. 1(a) presents the surface heights from one side of the seismogenic zone of the fault along an $x-y$ plane. As described in Selvadurai and Glaser (2017), the fault shows clear signs of wear, i.e. smooth, polished sections existed within a larger rougher region. From the micromechanical concepts mentioned before, we presume that due to local variations in roughness each region will express different sets of asperities that collectively govern the frictional behavior and are defined by different D_c values (Yoshioka, 1997; Marone and Cox, 1994). We will describe a *cutting plane method* that spatially discretizes the frictional properties to a planar fault using measurements inferred from the two (smooth and rough) surfaces defined by the bimodal Gaussian model of roughness observed in an associated experiment (Selvadurai and Glaser, 2017).

3. Previous laboratory roughness measurements

Roughness has been proposed as a controlling feature linked to variability in frictional behavior on faults (e.g. Scholz and Aviles, 1986). We briefly describe some methods used to quantify surface roughness on the interface presented in Fig. 1(a). Average roughness can be determined using the root mean square of surface height:

$$h_{rms} = \sqrt{\left(\frac{1}{N}\right)\sum_{i=1}^{N} h_i^2}, \tag{1}$$

where N is the total number of measurement points and h_i is the individual surface height. To estimate statistical properties of surface heights, the probability density functions (PDFs) of the surface height h defined by a Gaussian distribution, was used and is given as:

$$\phi(h) = (2\pi\sigma^*)exp\left[\frac{(h-\mu^*)^2}{2\sigma^{*2}}\right], \tag{2}$$

where μ^* is the arithmetic mean and σ^* is the standard deviation. Building on Eq. (2) the PDF for a bimodal Gaussian mixture model is given by

$$\Phi(h) = p\cdot\phi_1(h) + (1-p)\cdot\phi_2(h), \tag{3}$$

where p is the mixture ratio between the two Gaussian distribution functions ϕ_1 and ϕ_2, each with their individual means and standard deviations.

Fig. 1(b) displays the normalized probability distribution function for the entire surface. Gaussian (Eq. 2, magenta) and bimodal Gaussian

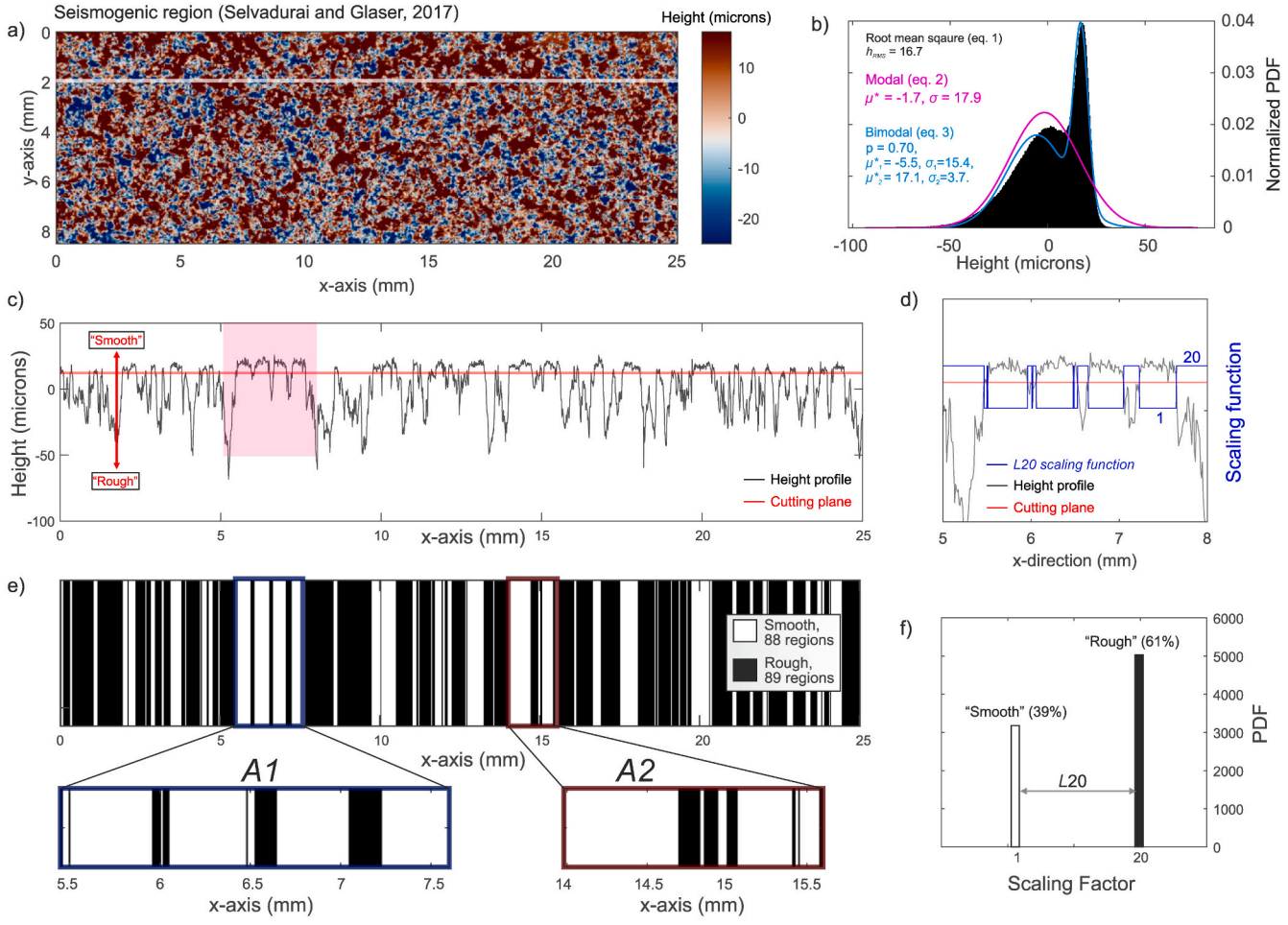

Fig. 1. **(a)** Surface roughness measurements of a worn section of the poly(methyl methacrylate) (PMMA) slider block using an optical profilometer (Selvadurai and Glaser, 2015; Selvadurai and Glaser, 2017). **(b)** Normalized surface height probability density function (PDF) for the entire 2-D surface in (a). Values of three surface roughness models are shown: root mean square, Gaussian (magenta) and bimodal Gaussian (cyan), in which the values are given in microns. **(c)** 1-D roughness profile (gray) taken from the transect at $y = 2$ mm in (a). The cutting plane is shown as the red line. **(d)** Small section of the height distribution showing the roughness profile (grey line), the cutting plane (red line) and the scaling function (blue line) for the $L20$ distribution. **(e)** Fault heterogeneity of the scaling function in a "barcode-style" representation determined from the cutting plane method described in Section 4.2. **(f)** PDF of the amount of smooth (white) to rough (black) sections in (e). The scaling function $SF(x)$ was shown for the level of heterogeneity $L20$.

(Eq. 3, cyan) distributions are shown graphically and the values of the means (μ^*), standard deviations (σ^*) and mixture ratio (p), are given with units of μm. The shape of the distribution is better represented by the bimodal Gaussian distribution by visual inspection.

4. Numerical model

We develop a method to characterize a complex frictional distribution that distinguishes between smooth and rough sections using experimental measurements of roughness (Fig. 1). The spatial distribution of smooth and rough sections of the fault is implicitly controlled by wear and directly modeled here. We use the binary representation of smooth and rough to prescribe low and higher values of D_c, respectively.

Using the rate- and state-dependent solver QDYN we study earthquakes sequences under heterogeneous distribution of D_c, while maintaining constant other parameters controlling friction (e.g. a, b and σ_n). This description implies that the fracture surface energy and weakening-rate vary spatially within the simulations (Ide and Aochi, 2005; Hillers et al., 2006; Hillers et al., 2007; Aochi and Ide, 2017; Noda et al., 2013).

4.1. Theoretical formulation

The phenomenological RSF constitutive friction law is derived from laboratory experiments (e.g. Dieterich, 1979). The model describes the behavior of a fault's resistance to sliding in terms of shear stress τ as a function of slip rate V and state variable θ. This is given as:

$$\tau(V,\theta) = \sigma_n\left[\mu + a\ln\frac{V}{V^*} + b\ln\frac{V^*\theta}{D_c}\right], \tag{4}$$

where σ_n is the normal stress, μ is the reference steady-state friction coefficient at an arbitrary reference slip rate V^*, D_c is the characteristic slip distance and a and b are constitutive parameters describing the direct and evolution effects, respectively. We adopt the state evolution in the form of the so-called "slip law":

$$\dot{\theta} = -\frac{V\theta}{D_c}\ln\frac{V\theta}{D_c}, \tag{5}$$

where steady state frictional stress $\dot{\theta}= 0$, is given as

$$\tau_{ss}(V) = \sigma_n\left[\mu + (a-b)\ln\frac{V}{V^*}\right]. \tag{6}$$

The "ageing law" is another commonly used state evolution law; however, we choose the slip law because of its ability to model other laboratory studies (Kaneko and Ampuero, 2011; Kaneko et al., 2016). For $(a-b)\langle 0, \tau_{ss}$ will decrease as slip rate V increases. A fault with these characteristics is known as velocity-weakening (VW) and may develop instability if the fault stiffness is below a critical stiffness. For the VW spring-slider system, Ranjith and Rice (1999) found the critical stiffness to be:

$$k_{cr} = \frac{\sigma_n(b-a)}{D_c}. \tag{7}$$

This implies that quasi-static steady-state slip is stable ($V\rightarrow V^*$) or unstable ($V\rightarrow\infty$) if the spring stiffness is greater or less than the critical value k_{cr}, respectively. Critical fault stiffness is inversely proportional to the minimum half-length of a nucleation zone capable of instability:

$$L_c \sim \frac{G' D_c}{(b-a)\sigma_n}, \tag{8}$$

where the effective shear modulus $G'(= G/(1-\nu))$ is used for the Mode II plane strain problem and ν is the Poisson's ratio (Rubin and Ampuero, 2005).

The equation of motion controlling slip in the quasi-dynamic approximation is given by:

$$\tau_{el}(\mathbf{x}) - \tau(\mathbf{x}) = \frac{G'}{2V_S}V(\mathbf{x}), \tag{9}$$

where τ_{el} is the elastostatic shear stress due to the loading boundary condition (Horowitz and Ruina, 1989). The inertial term of Eq. (9) represents the radiation damping term for S waves produced along the fault at point $\mathbf{x}$, which expands at speeds closer to the shear wave speed V_S of the material (e.g. Rice, 1993).

Rubin and Ampuero (2005) showed that the common length scale

$$L_b \equiv \frac{G' D_c}{\sigma_n b}, \tag{10}$$

controls aspects of earthquake nucleation and the transition from aseismic to seismic behaviour. This transition threshold velocity is defined as:

$$V_{dyn} = \frac{2aV_s\sigma_n}{G'}, \tag{11}$$

which represents the transition point where the inertial term in Eq. (9) becomes significant (Rubin and Ampuero, 2005).

Quasi-static interactions between fault elements are calculated using the boundary element method (BEM) and all calculations reported in this study were solved using a Quasi-DYNamic (QDYN) earthquake simulator (Luo et al., 2017a). QDYN solves the equation of motion given in Eq. (9) using the numerical method for the quasi-dynamic solver described in Rubin and Ampuero (2005, see Section 2 therein). The validity and benchmarking of QDYN was also verified by Erickson et al. (2020). Solution convergence and mesh discretization of the heterogeneous models, described later, are further elaborated in Supplemental Methods S2.

4.2. Cutting plane method

The *cutting plane method* splits the roughness patterns into two separate sections: smooth and rough. Using this method, we assigned binary sets of frictional parameters to both the smooth and rough regions of the roughness profile. A 'cutting plane' was defined to be exactly between the two means of the bimodal distributions. In this study, we build a simple 1-D model and arbitrarily examine the transect of roughness at $y = 2$ mm. Fig. 1(c) displays the roughness along x at $y =$ 2 mm (black line). The cutting plane (red line) was defined as $h_{cut} = (\mu_1^* + \mu_2^*)/2$ for surface heights along the transect at $y = 2$ mm, where μ_i^* are the means of the bimodal Gaussian distributions discussed in Section 3.

A scaling function, SF(x), is used to partition the smooth and rough sections of the fault. Fig. 1(d) presents a detailed view of the roughness (black), the cutting plane (red) and the scaling function (blue). When roughness was above the cutting plane the scaling function was unity. All heights below the cutting plane were prescribed as scaled values. This allowed us to control the magnitude, or level of heterogeneity in fracture energy (toughness).

To map the spatial fluctuations in D_c over the fault, the smooth value of critical slip distance was multiplied by the spatially varying scaling function ($D_c(x) = D_{c,low}\cdot\mathrm{SF}(x)$). The magnitude of D_c in the rough sections depended on the level of the scaling function. For example, for level $L20$, the larger critical slip value was $D_{c,high} = \max[D_c(x)] = 25$ nm$\cdot$ $20 = 500$ nm $= 0.5$ μm. The choice of $D_{c,low}$ is discussed in Section 4.3.

The scaling function produced heterogeneity in two ways: (*i*) spatial variations are controlled by the location where the experimental roughness profile crossed the cutting plane, and (*ii*) the level of heterogeneity, i.e. the peak-to-peak range of scaling function, which is chosen by the modeler. Fig. 1(e) shows the spatial heterogeneity in terms of a "barcode" representation of the scaling function. The

probability distribution function (PDF) of the level $L20$ scaling function is given in Fig. 1(f).

4.3. Frictional parameter space

Table 1 presents the baseline frictional, material and length scale parameters used in this study. Proper fault meshing for the numerical simulations is needed to correctly capture the dynamic processes at the rupture tip. Mesh size was estimated in terms of the common length scale L_b (Eq. 10). To accurately capture local frictional breakdown it was necessary to apply a maximum grid size of $\Delta x/L_b < (1/50)$ for our choice of $a/b = 0.65$. We used $2^{13} = 8192$ grid points over the length $L = 25$ mm of the mesoscopic domain, resulting in a resolution $\Delta x \sim 3$ μm.

Two assumptions are taken from previous experimental studies to choose our model parameters: (1) Asperity normal stress, measured using the calibrated pressure film (Selvadurai and Glaser, 2015), could attain normal stresses σ_n up to 25 MPa and (2) surface roughness estimates in Selvadurai and Glaser (2017), found that polished sections produced nanometrically smooth roughness, whereas rough sections had roughness on the micron level. It has been hypothesized that the root mean roughness h_{rms} (Eq. (1)) may be related to critical slip distance (Baumberger and Caroli, 2006; Yoshioka, 1997), which explains our choice of $D_{c,low} = 25$ nm in all the simulations.

5. Computational results

Our model considers tough barriers populated with fragile/brittle asperities due to the variations in fracture energy G_c along the fault (Ide and Aochi, 2005; Noda et al., 2013; Aochi and Ide, 2017). Tough/rough regions ($D_{c,high}$) present relative barriers due to their higher resistance to frictional breakdown. Brittle/smooth regions that had $D_{c,low}$, exhibited lower levels of fracture energy G_c and were stiffer according to Eq. (7). This increased stiffness made them prone to nucleate localized seismicity as they load more quickly to their peak strength. Using the rate-and-state framework and the consequences of the heterogeneous distributions of the state evolution distance, earthquake sequence simulations were used to investigate complex precursory frictional phenomena during the seismic cycle.

Table 1
General model parameters used in the 1-D RSF models.

Parameter	Symbol	Value
Shear modulus	G	2.39 GPa
Poisson ratio	ν	0.32
Shear wave speed	V_S	1330 m s^{-1}
Reference friction coefficient	μ^*	0.6
Reference slip rate	V^*	0.1 μm s^{-1}
Dynamic sliding threshold	V_{dyn}	0.177 m s^{-1}
Loading plate velocity	V_{LP}	0.1 μm s^{-1}
♣Lower critical slip distance	$D_{c,low}$	25 nm
Heterogeneous critical slip distance	$D_c(x)$	$D_{c,low}\cdot$ SF(x)
♠ Normal stress	σ_n	25 MPa
†Length of mesoscopic domain	L	25 mm
† Height of mesoscopic domain	H	2.5 mm
Width of mesoscopic domain	W	∞
Grid size	Δx	3 μm
Grid points	n	2^{13}
★"Evolution" effect	b	0.0144
★"Direct" effect	a	0.00936
Critical nucleation length	$(L_c)_{low}$	0.498 mm
Common length scale	$(L_b)_{low}$	0.166 mm
Simulation time	t_{sim}	600 s
Level of heterogeneity	L	1, 10, 15, 17.5, 20

♣ Roughness measurements (Selvadurai and Glaser, 2017).
♠ Pressure sensitive film measurements (Selvadurai and Glaser, 2017).
★ Studies on PMMA-PMMA interfaces (Berthoude et al., 1999).
† Discussed in Supplement Section S1.

5.1. General observations

In Fig. 2(a), we compare the maximum slip rate on the fault for the homogeneous $L1$ and heterogeneous $L10$ fault. Each numerical simulation lasted for $t_{sim} = 600$ s, which allowed for the "burn in" phase that is typical in these types of numerical models (e.g. Hillers et al., 2006). The homogeneous case (gray line) shows the typical smooth response where an interseismic period is followed by a preseismic (nucleation) phase. This is followed by full coseismic rupture that propagates and arrests with a post-seismic relaxation phase. The definitions for these phases are explained in detail in Appendix A2.1, A2.2 and A2.3 in Rubin and Ampuero (2005) in relation to the behavior of the one-dimensional spring-block slider cycles with radiation damping. The transition between postseismic and interseismic phase begins at the inflection point where slip rate goes from decreasing to increasing. The interseismic phase is concluded and the preseismic (nucleation) phase begins when steady state is reached (Eq. (6)). The coseismic phase is defined when the slip rate at any place on the fault exceeds the dynamic slip rate V_{dyn} (Eq. (11)).

During the interseismic period, slip rates on the fault are below the loading plate velocity (V_{LP}). For the homogeneous faults, the coseismic phase meant that slip-rates exceeded V_{dyn}, resulting in full ruptures. A full rupture is described as one that dynamically breaks all computational nodes before arresting due to the periodic boundary conditions. Periodic boundary conditions assume that distributions of frictional heterogeneity is applied all along an infinite fault and the spatial distributions are periodic with spatial period L (Luo et al., 2017a).

In Fig. 2(a), the behavior of the $L10$ case displayed less locking, that is, the maximum slip velocity on the fault during the interseismic period is larger (approximately two orders of magnitude) than for the homogeneous $L1$ case. This decrease in fault locking was also noted in RSF simulations that shows the fault response for increasing fault roughness explicitly (Tal et al., 2018; Cattania and Segall, 2021). In Supplementary Section S4, we show the fault response for each level of toughness heterogeneity. We see that the level of locking decreased with an increasing level of toughness heterogeneity. At the highest level of toughness heterogeneity ($L20$), the fault is creeping at $\sim V_{LP}$ with small localized seismic events that do not cause or participate in larger ruptures in the surroundings.

In Fig. 2(b), we examine the spatio-temporal slip velocity evolution in the highlighted times between $t = 300$ s to 350 s for the heterogeneous $L10$ case. For comparison, the lower panel shows the slip velocity evolution for the homogeneous ($L1$) model. For the heterogeneous $L10$-model, we see that the model produced a wide variety of behaviors from widespread accelerated preslip, localized slow slip events, burst-like seismicity and the nucleation of a mainshock. On the right hand side, we show the associated 'barcode' distribution of frictional heterogeneity from Fig. 1(e) for reference. The red-stars indicate the location where seismic slip initiated.

In Fig. 2(b), we have highlighted two asperities $A1$ from $x \in$ [5.45, 7.6] mm, and $A2$ from $x \in$ [14.0, 15.6] mm (white lines). The size of each asperity was $L_{A1} = 2.15$ mm and $L_{A2} = 1.6$ mm. In Fig. 1(e), their composition is highlighted in the inset images. These two asperities represented larger sections of mostly smooth sections and are discussed in more detail in Section 5.4. These asperities displayed the most relative locking for all cases and were responsible for the majority of the seismicity. In Fig. 2(b), we show that these asperities produced sequential bursts of seismicity ($A2$ followed by $A1$), followed by sequential slow slip events ($A2$ followed by $A1$), which lead to the mainshock nucleating from the edge of the relatively locked $A1$ asperity. These two asperities produced a wide range of complexity and seismicity in all models – only in $L20$ was the $A2$ asperity seismically inactive.

The maximum slip rate with respect to time is given for each heterogeneous model for the entirety over the full simulation (see Supplemental Section S4). We see that the recurrence interval between

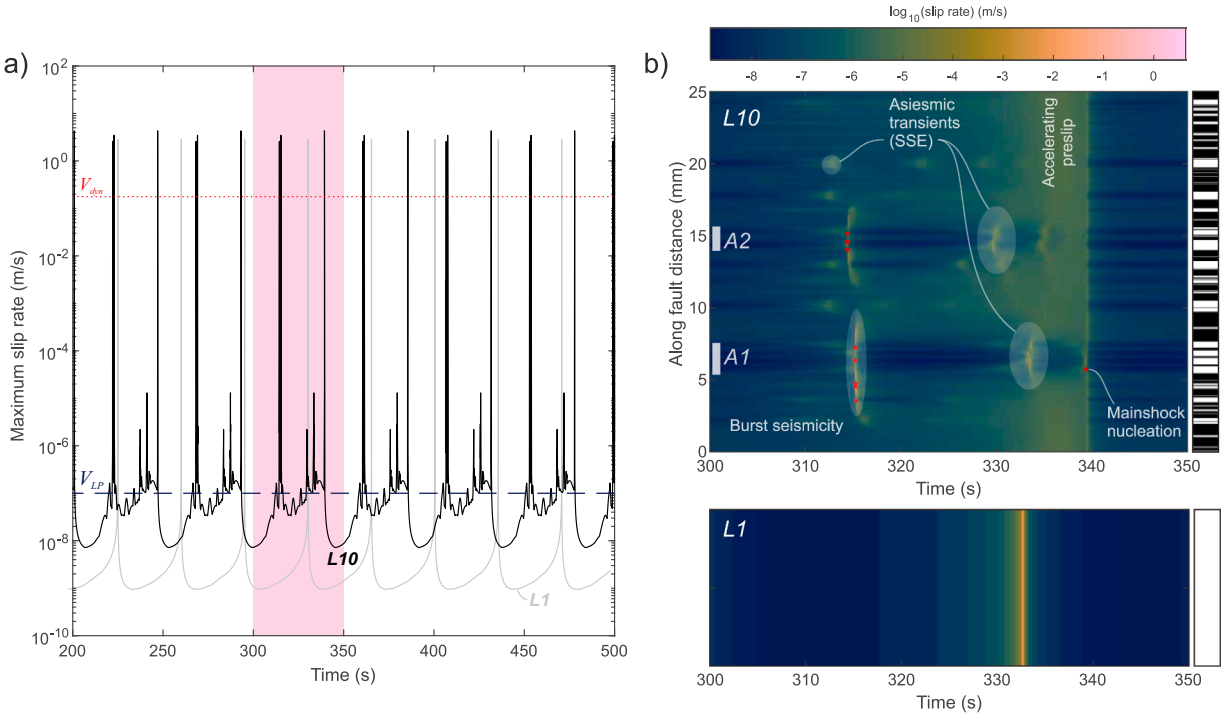

Fig. 2. **(a)** Maximum slip velocity over multiple cycles on a heterogeneous $L20$ (black) and homogeneous $L1$ (gray) fault. The dynamic slip rate threshold V_{dyn} is shown for reference. **(b)** Spatio-temporal distribution of slip velocities along the fault for one cycle is highlighted for the $L10$-model. A range of behavioral patterns were observed including burst seismicity, slow slip events, accelerated creep and mainshock nucleation. Two asperities (A1 and A2) are highlighted as they represented regions that showed higher levels of locking with respect to their surroundings for all models considered (see Supplemental Section S4). The barcode distribution of frictional properties is given for reference. The red stars represent positions on the fault that suddenly breached the dynamic threshold. The lower panel shows the spatio-temporal slip velocity evolution for the homogeneous ($L1$) model.

mainshocks decreases as the strength heterogeneity becomes larger. However, full ruptures begin to arrest with increasing strength of the barriers producing "partial ruptures" for the $L15$ and $L17.5$. This is discussed in more detail in Section 5.2. At the highest level of strength heterogeneity ($L20$), there we no mainshocks and only the dominant asperity $A1$ produced seismicity. For this case, the average shear stress was higher and fluctuated near the shear strength of the homogeneous model. The average shear stress with respect to time is given for each heterogeneous model over the full simulation in Supplemental Section S4.

5.2. Transition to the preseismic (nucleation) phase

We examine the unlocking sequences that lead to a larger mainshock in our simulations for different levels of toughness heterogeneity. Full ruptures break the entire fault ($L_{rup} = L = 25$ mm) and only the homogeneous $L1$ and $L10$ cases produced this response. As the level of toughness was increased, only partial rupture were observed for the $L15$ and $L17.5$ models. Partial ruptures were defined as ruptures that propagated over at least 40% of the fault extent ($L_{rup} = 0.4 \cdot L \geqslant 10$ mm). This size was chosen arbitrarily, but allowed us to study the unlocking sequences prior to larger ruptures in the simulations.

Dieterich (1992) studied the simple patch model and found the velocity of the patch during nucleation scales as a function of time-to-failure as $V_{patch} \propto 1/t_f$. Noda et al. (2013) examined the effect of this scaling behavior with the presence of small fragile asperities embedded in a tough larger barrier, which is the same mechanism studied here. They found that the small asperities had the propensity to promote faster rates of nucleation depending on their condition, i.e., by increasing the creep rate and decreasing the strength of the adjacent tougher regions.

Fig. 3 looks at the influence of the level of toughness heterogeneity on the partial and full rupture sequences and compares it to the acceleration of the slip in the homogeneous model. The left panels show the spatio-temporal distribution in slip velocity for a representative full or partial rupture event. We display the influence of increasing the fault toughness on nucleation behavior for the $L10$ (Fig. 3(a)), $L15$ (Fig. 3(b)) and $L17.5$ (Fig. 3(c)) cases. The right panels display the acceleration of the fault slip prior to the larger events. The homogeneous model $L1$ is shown for reference (dark blue line), in which time-to-failure follows the $1/t_f$ scaling (various dashed lines). We define the initiation of earthquakes, i.e. time-to-failure $t_f = 0$, as the time when the maximum slip rate becomes larger than V_{dyn} for the homogeneous $L1$-model. The horizontal axis in the right panels of Fig. 3 are related to the $L1$ solutions and the overlaid response for heterogeneous models are for comparison to the $L1$-model. The dynamic slip rate threshold (V_{dyn}) and loading plate velocity (V_{LP}) are shown for reference. The inset plots on the right hand side depict the PDF of the rupture lengths being analyzed. For example, the inset image in for the $L10$ model (Fig. 3(a)) shows that all large ruptures were full ruptures ($L_{rup} = 25$ mm). In the $L15$-model only partial ruptures ($L_{rup} \sim 17$ mm) were produced and studied.

5.2.1. L10-model

The $L10$-model in Fig. 3(a) displayed acceleration of $1/t_f$ leading to ruptures that spanned the entire fault. We see that the fault initially accelerates faster than $1/t_f$ but then slows down (white arrow) approximately 1 ms before the mainshock achieves seismic slip rates. From the spatio-temporal distribution of slip rate, this bump appears to be associated with small contrasts in heterogeneity on the predominantly smooth $A1$ asperity. The composition of the dominant asperities is discussed in Section 5.4. These smaller tough regions in the vicinity of the nucleation front on the $A1$ asperity impose small barriers that affect smooth nucleation but not to a significant degree. Once the nucleation

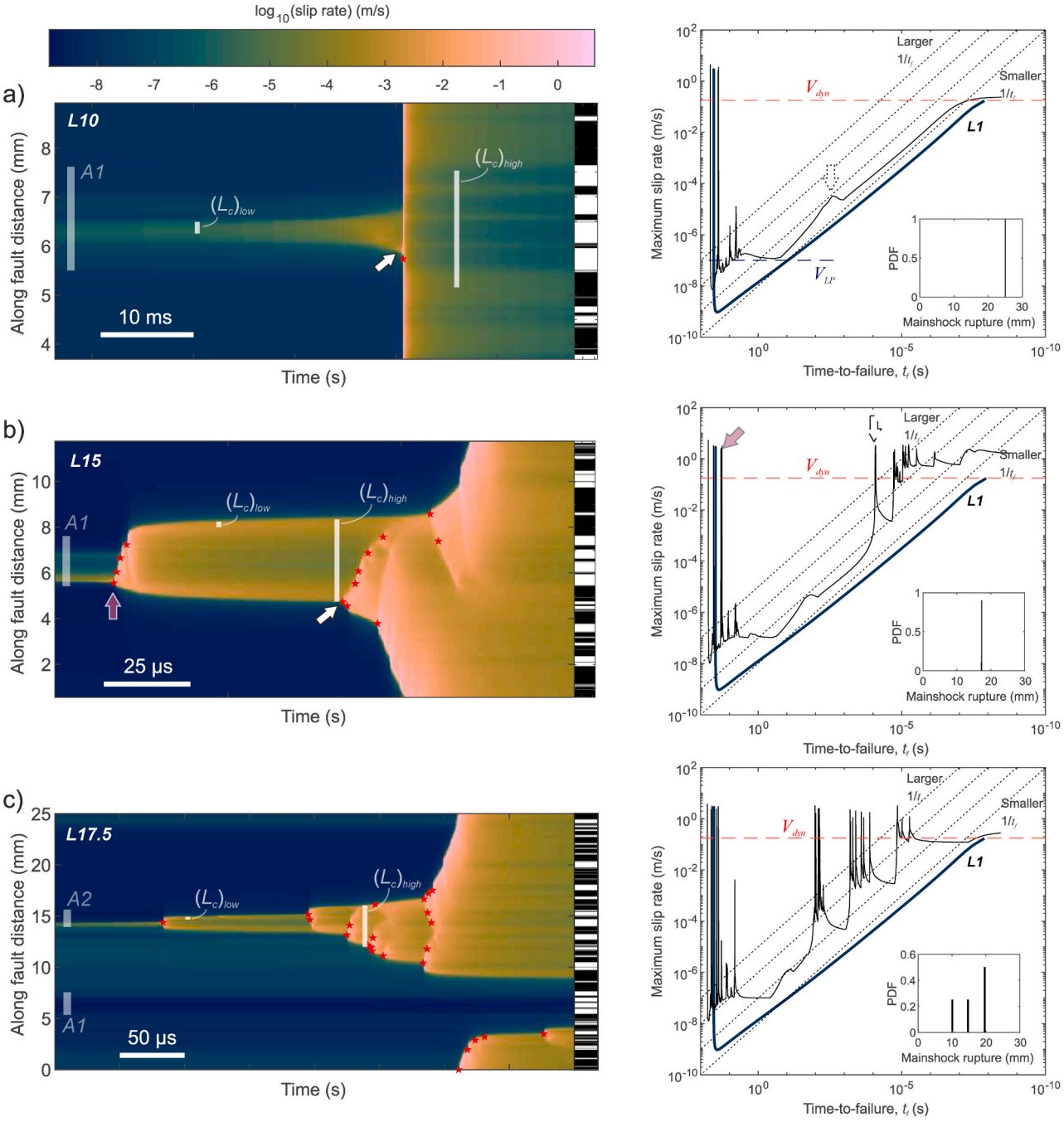

Fig. 3. (Left) Spatio-temporal evolution of slip rates on fault for a large full or partial rupture event (see text for definition). Eq. (8) was used to calculate the minimum and maximum L_c for the smooth and rough sections, respectively. (Right) Acceleration of the fault slip prior to the initiation of large full or partial ruptures. The black line represents the case visualized on the left. The homogeneous $L1$ model is shown for reference. Nucleation sequences are shown for the **(a)***L*10-model, **(b)***L*15-model and **(c)***L*17.5-model. The arrows are described in the text.

front breaches these localized barriers, nucleation accelerates smoothly as $1/t_f$ in the homogeneous case. The hypocenter of the mainshock was at the edge of the smooth-tough boundary of the $A1$ asperity for all large events in our simulations.

5.2.2. *L*15-*model*

Fig. 3(b) shows the nucleation behavior response as the toughness heterogeneity was increased to $L15$. The left panel reveals that unlocking of the fault occurred in a more chaotic manner with many events on the $A1$ asperity in close proximity to the eventual hypocenter. We see that within the $A1$ asperity, the small tough sections can now inhibit the dynamic rupture front locally, leading to incremental unlocking of the asperity via a burst of smaller events (purple arrow, LHS 3(b)). Stress transfer during the burst events (discussed below) lead to sequential unlocking of the $A1$ and $A2$ with seismicity that migrates in space. This migration can also lead to repeated sequences later on in the cycle and also a reversing of the event sequence depending on the condition (strength and slip rate) of regions surrounding the dominant asperities.

In Fig. 3(b), we see that acceleration follows a $1/t_f$ scaling similar to the homogeneous case. However, at $t_f \sim 10^{-4}$ s, a precursory event was observed (white arrow) that caused an earlier onset of mainshock nucleation (Noda et al., 2013). This behavior has been proposed by a

rate-dependent cascade-up model (Noda et al., 2013; McLaskey, 2019), where foreshocks, occurring in a preslip region, are triggered by aseismic loading; however, stress perturbations can then prompt the nucleation of runaway rupture and the mainshock. The fault initially obeys the preslip model but when the fault is at a near critical state, the local foreshock can trigger a cascading process.

Using Eq. (8) and substituting $D_{c,high} = 0.375$ μm, we obtain an $L_{c,high} = 3.6$ mm as the critical nucleation length-scale on the rough sections. This is shown for reference in the right side of Fig. 3(b). We clearly see that after the burst of seismcity on the $A1$ asperity, the adjacent tough regions in the wake of theses events begin to slide faster. Also, the preslip region expands slightly to a region larger than the $A1$ asperity but equal to the critical nucleation length for the rough regions. Once the preslip region of the representative section has almost reached the larger nucleation length, it begins to nucleate but at an earlier time than homogeneous $1/t_f$ acceleration, essentially pushing forward the onset of the larger event. This behavior is hypothesized by the *rate-dependent cascade-up model*. This was not observed in the $L10$ case. This behavior is likely linked to the increased ability of the fault to keep the foreshock "kicks" somewhat constrained, to allow a nucleation region to form in the tougher regions at longer length scale $L_{c,high}$, in the region surrounding the predominant $A1$ asperity.

5.2.3. *L*17.5-model

Fig. 3(c) shows the nucleation associated with the $L17.5$ case. We note that the fault started to behave more chaotically; the larger ruptures ranged from 10 mm to 20 mm and showed complex acceleration patterns. Similar to the $L15$ model, small foreshocks were present and were a by-product of aseismic loading within the nucleation region of the rougher barrier. These foreshocks accelerated the adjacent sliding region until the accelerated sliding region grew to the critical nucleation size for the rough section, which was $L_{c,high} = 4.1$ mm for the $L17.5$ case. At this point foreshocks are more prevalent and their "kicks" into the adjacent rough sections are more easily constrained/arrested so that perturbations to the system are less apparent than the $L15$ case. However, the system eventually reaches a critical state, in which enough preslip has localized at the larger nucleation length scale at this point, the subsequent "kicks" from the foreshock will trigger the larger event at an earlier time.

5.3. Seismicity sequences during the interseismic phase

The asperities $A1$ and $A2$ showed burst-like seismicity during the interseismic phase (see Fig. 2(b)), except the $L20$-model (discussed later). The $A1$ and $A2$ asperities displayed frictional interplay between each other. There were alternating sequences of bursts or even slow slip seismic events as the fault became progressively weakened. The seismicity on the brittle patches occurred incrementally and gradually increased the slip rate and decreased the stress in the tough, adjacent barriers. This behavior was also seen in other numerical simulations for modeling tough asperities with local, smaller brittle features (Ide and Aochi, 2005; Aochi and Ide, 2014; Noda et al., 2013). Progressive breakdown of shear stress through slip has also been proposed to explain the unlocking of other laboratory friction experiments (Rubinstein et al., 2004; Maegawa et al., 2010; Ke et al., 2018; Selvadurai et al., 2017). The spatio-temporal evolution of slip for a cycle is presented in Fig. 2(b) for the $L10$ case and in the Supplement Section 4 for all other models.

We do not examine the nucleation behavior on the $L20$ model since the seismcity generated on asperity $A1$ were fully contained by the tougher surroundings that were sliding at rates closer to the loading plate velocity V_{LP}. The $L20$ model produced a repeater-like response in the dominant $A1$ asperity (see Supplemental Section S4). The relative locking of this asperity was alleviated via localized seismcity that allowed the slip deficit to be recovered to the surrounding region sliding at $\sim V_{LP}$. Our model for this repeater-like behavior is produced entirely on velocity-weakening fault sections with varied toughness. This differs from RSF formalizations to reproduce repeating earthquakes in nature; i.e. a circular asperity embedded in velocity-strengthening surroundings (e.g. Chen and Lapusta, 2009). While it is beyond the scope of this study, differences (e.g. recurrence time) between the two formalizations may be an interesting point for further study.

5.4. Properties of the dominant *A*1 and *A*2 asperities and bursts of seismicity

All simulations showed that most seismicity is produced on the two dominant asperities $A1$ and $A2$. The composition of these asperities are shown in detail, in the subset images of Fig. 1(e). They consisted of regions with relatively large amounts of smooth/brittle ($D_{c,low}$) regions with relatively smaller amount of delimiting tough sections. Over the whole fault the spatial roughness ratio $R_{S/R} \sim 2{:}3$, which is the ratio of smooth to rough regions. On both the dominant asperities (A_1 and A_2) this ratio $R_{S/R} \sim 4{:}1$. In our formulations the concept of a roughness ratio can be interchanged with brittle:tough. We believe this difference in spatial distributions is the explanation for their complex response and these were not defined or prescribed by the modeler but by the physics governing what created the roughness profiles used in this study (i.e. wear).

5.5. Validation using seismic source physics

Our first validation method of the numerical results was to compare the source properties of the localized events procured in an independent manner. Selvadurai (2019) used kinematic models (e.g. Brune, 1970) to estimate source radius a_r and seismic moment M_0 from seismically produced ground motions measured using a calibrated array of broadband acoustic emission sensors. Fig. 4(a) shows the estimates made using the kinematic approach for both P and S waves. We have superimposed the source estimates made from the kinematic approach onto estimates of scalar seismic moment and rupture length scale from our simulations. How the individual source features are determined in this study is detailed in Supplementary Section S3. From our simulations, we estimate the seismic moment as $M_0 = \mu A_r s$, where s is the average slip over the rupture area $A_r = L_{rup}^2$. This assumption has been validated so long as the dynamic ruptures do not break the full extent of the fault (Luo et al., 2017b). The seismic moment of the full rupture events are no longer valid in the 1D approximation according to Luo et al. (2017b). This explains the deviation from the $M_0 \propto A_r^{3/2} \propto L_{rup}^3$ scaling for the larger events in Fig. 4(a). Those events are not considered for the comparison to the kinematic estimates made by Selvadurai (2019). Kinematic models use the spectral response of ground motion and relate the low-frequency displacement plateau and corner frequency of the specific wave phase to estimate the scalar seismic moment and source radii, respectively.

The classical empirical scaling relationship between seismic moment and source geometry ($M_0 \propto L_{rup}^3$) is also shown and both data sets follow the trend. Deviations from the $M_0 \propto L_{rup}^3$ scaling was observed for larger full rupture events that broke the entire fault as predicted by Luo et al. (2017b). Stress drop was also calculated in our model and was relatively constant $\sim$ 1.86 MPa. In Fig. 4(a), the computational results show an overlap with kinematic estimates confirming the plausibility of our model. There are a number of limitations to the kinematic approach, e.g. reliable sensor bandwidth and model assumptions that can lead to the observed spread as mentioned in Selvadurai (2019).

5.6. Validating the rates of slow rupture expansion

Fig. 4(b) presents the interseismic phase of the $L17.5$-model where the white line represents a marker that indicates the maximum slip rate

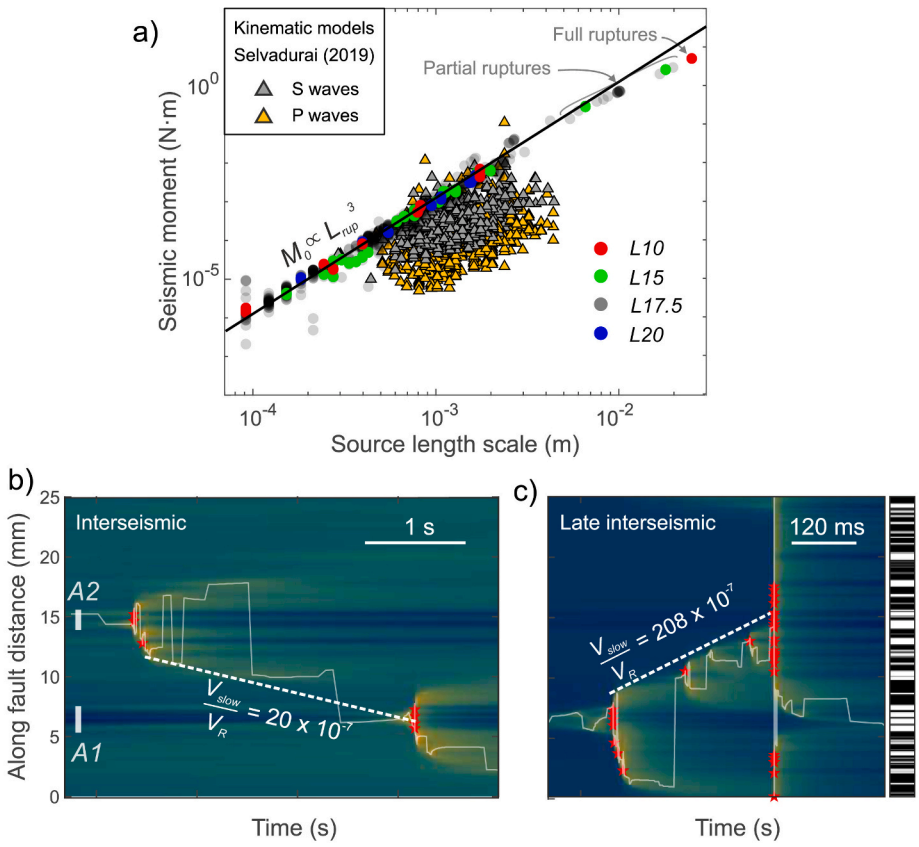

Fig. 4. **(a)** Comparison of source features of the localized seismicity in all models to the kinematic estimates from the experimental measurement made by Selvadurai (2019). **(b)** Enhanced view of the burst events on asperities $A2$ and $A1$ during the interseismic phase. The dashed white line estimates the rate between the last event on $A2$ and the first event on $A1$, normalized by the Rayleigh wave speed of the material. **(c)** Enhanced view of the premonitory phase as the fault prepares for a larger event. The dashed white line tracks the outside of the growing preparatory preslip front. Both (b) and (c) are taken from a seismic cycle from the $L17.5$-model. The location of the maximum slip rate on the fault is traced by the thin white line at any moment in time. The same color scheme indicating the logarithm of slip rate is used as in Fig. 2.

along the fault throughout the faults spatio-temporal evolution. In Fig. 4 (b) we zoom in and visualize the time between the seismic burst events that occurred on $A2$, then subsequently $A1$, during the interseismic phase. The time between the last event on $A2$ and the first event on $A1$ is $\sim$ 2.7 s and over a distance of 6.5 mm, which represents a propagation speed of $\sim$2.4 mm/s. We then normalize this rate by the Rayleigh wave speed of the material $V_{slow}/V_R \sim 20 \times 10^{-7}$ (where $V_R = 0.93V_s$ for PMMA) to facilitate quantitative comparisons. The reason for normalizing this value will be discussed later.

Fig. 4(c) shows the breakdown phase leading up to a larger partial slip event as the fault prepares for a mainshock. Here, it is more evident where the aseismic slow slip front extends due the addition of accelerated preslip as the fault prepares to nucleate a larger scale event. The contrast between the relatively locked regions and the creeping surroundings are shown with the white dashed line. By performing the same estimates for the expansion rate of this preparatory region, we find that it expands at $V_{slow}/V_R \sim 208 \times 10^{-7}$.

By normalizing these expansion rates in our models, we can compare the results to estimates from laboratory experiments in identical settings (Selvadurai et al., 2017). Using the non-contact "creep-sensors" that straddled the experimental fault (see Supplemental Fig. S1c), Selvadurai et al. (2017) were able to experimentally track a slow aseismic rupture front and found its velocity to range between $V_{slow}/V_R \in [5,172] \times 10^{-7}$. They also noted that the expansion rate of the slow rupture also accelerated prior to stick–slip events, as was found in our model.

The dashed lines in Fig. 4b represents an average value of the propagation speed. Close inspection reveals that slow slip migrates towards $A1$ first, then after some time delay, a seismic failure occurs at $A1$. This appears to follow hypotheses by Bartlow et al. (2011) who linked Episodic Tremor and Slip (ETS) to slow slip events in central Cascadia. In nature, slow slip events (SSEs) are tracked by the expression of seismicity (e.g. Kato et al., 2016) or/also using geodetic approaches (e.g. Passarelli et al., 2021). Catalogs of the slow slip events are shown to migrate at velocities between $\sim$1 km/day and $\sim$20 km/day (Passarelli et al., 2021). Assuming a Rayleigh wave speed $V_{R,rock} = 3094$ m/s (granite), we calculate the expansion of SSE in nature, which range from $V_{SSE}/V_{R,rock} \in [37, 748] \times 10^{-7}$, which is comparable to both those observed experimentally (Selvadurai et al., 2017) and the numerical results presented here.

6. Discussion

Our model provides a deeper understanding of seismic/aseismic slip interactions at a laboratory scale and improves on the planar fault approximation and its relationship to realistic sliding surfaces (in our case, for a worn surface). RSF's ability to model laboratory nucleation processes (Kaneko et al., 2010; Kaneko et al., 2016) has benefited from increased spatio-temporal resolution of experimental observations (Nielsen et al., 2010; Latour et al., 2013), which allow for validation and better understanding of the validity of the phenomenological friction law. However, these studies have not been able to account for a wide variety of preparatory slip phenomena, such as foreshocks, measured by acoustic emission sensors, that have been experimentally observed in the late interseismic phase.

Heterogeneity on natural faults relies on the inherent discreteness of the models and may act as a tuning parameter to match fault dynamics but should, to some degree, verified using laboratory experiments when possible. While it is not clear if the planar fault model presented here, with a 'barcode-style' distribution of D_c, produced by wearing and polishing of local sections of the fault, is directly appropriate to upscale to complex fault settings (e.g. Cocco et al., 2023), this may give insight into distributions of frictional heterogeneity at a local scale that can produce complex, realistic and validated precursory responses. Geologic observations of smooth and polished fault mirrors (FM) may be geologic

analogs that produce similar distribution of frictional properties studied here and may potentially be related to the work described here.

6.1. Could similar smooth/brittle patches exist in nature?

The presence of fault-mirrors observed on natural outcrops have sparked interest from the geophysical community (Fondriest et al., 2013; Kirkpatrick et al., 2013; Siman-Tov et al., 2013). Laboratory experiments have been crucial in understanding the mechanism surrounding the formation of fault-mirrors and in the debate on whether the presence of a fault-mirror can be used as an indicator of seismic slip (Fondriest et al., 2013; Siman-Tov et al., 2013; Pozzi et al., 2018). Fault mirrors have also been reproduced during slow slip (Tisato et al., 2012; Siman-Tov et al., 2015), in high-temperature environments (Pluymakers and Røyne, 2017) and even observed along glacial boundaries (Siman-Tov et al., 2017). The mechanisms controlling how surfaces polish and fault-mirrors develop on rock-rock interfaces and how they evolved on the PMMA surface presented here will differ. However, we were more interested in how the initial conditions of a worn, smoother surface embedded in a rougher fault could be used to construct a model that simulates a tough barrier with embedded smaller brittle patches. It has been proposed that the smooth layer caused by the deposition of nanoparticles during wear could retard healing, promoting the localization of slip that affects seismicity (Goldberg et al., 2016). These hypotheses could benefit from laboratory studies, specifically in the seismic response of mirror surfaces on geomaterial interfaces.

6.2. Potential bi-modal fractal description of frictional properties

Our model was developed from the observation that surface roughness was the direct consequence of a bi-modal Gaussian distribution of surface roughness due to wear. Evolution of roughness from Gaussian to bimodal Gaussian can be quantified using the polish-rate decay (wear decay) function (Adachi and Kato, 2000; Borucki et al., 2004; He et al., 2017; Hu et al., 2019); this evolution of roughness has been well-documented in the field of tribology. As the surface wears it reaches a steady state roughness and additional wear becomes negligible so long as the loading conditions remain constant (Adachi and Kato, 2000; Borucki, 2002; Borucki et al., 2004). Wear produces the distinct 'tail' in the PDF, and wearing of the interface can result in the genesis and growth of polished surfaces within the original roughness profile. New research into fractal characterization of such surfaces by Hu et al. (2019) suggests that a bi-modal fractal distribution in roughness is more representative of surfaces that exhibit this type of wearing (Leefe et al., 1998; Pawlus, 2008). These surfaces have already been shown to influence the characteristics of acoustic emission energy release upon sliding (Fan et al., 2010; Hu et al., 2019) but these results are recent and more investigation is required.

Bi-modal Gaussian and bi-modal fractal stochastic descriptions of frictional parameters would be an interesting avenue to investigate, specifically the role they play in nucleation sequences but also on the statistical properties of the earthquakes, for example frequency-magnitude distribution (FMD) (e.g. Wiemer and Wyss, 2002). Numerical studies have looked at earthquake cycles due to Gaussian distributions of D_c (Hillers et al., 2006; Hillers et al., 2007) but also, e.g. power law distributions in fault strength (Ripperger et al., 2007). To our knowledge up-scaling a bi-modal fractal power law distribution of frictional heterogeneity has not been investigated but may provide insight into processes that do not follow typical power law distributions (i.e. Gutenberg-Richter) of seismicity (Mignan et al., 2020).

6.3. Hierarchical rupture of dominant asperities

Hierarchical rupture is a phenomena explaining certain seismic observations in the Naka-Oki region in eastern Japan (Okuda and Ide, 2018; Okuda and Ide, 2018) and the Tohoku–Hokkaido subduction zone, Japan (Ide, 2019). Okuda and Ide (2018) studied seismograms that showed clear evidence of almost identical growth processes shared by repeating earthquakes of various sizes. They hypothesize that a hierarchical fault structure exists (as depicted in Fig. 5 of Okuda and Ide, 2018) and may be linked to heterogeneity in fracture energy, which is specifically the heterogeneity employed in this and others studies (Ide and Aochi, 2005; Noda et al., 2013; Aochi and Ide, 2017). Our model shows seismic complexity that shares certain similarities to the seismic response observed in Japan. In our model, the $A1$ and $A2$ asperities could represent some similar structure, in our case imposed by wear, which produced a wide myriad of seismic behaviors (Fig. 2(b)) but also possessed the potential to initiate runaway rupture (Fig. 3) similar to their up-scaled observations. These asperities were identified to have a substantially different roughness ratio $R_{S/R} \sim 4{:}1$ than the bulk of the fault ($R_{S/R} \sim 2{:}3$). They were seismically active in the interseismic phase (Fig. 2)) and their repeated seismic expression progressively weakened the fault, which is similar to those observed in other laboratory experiments (Rubinstein et al., 2004; Maegawa et al., 2010; Selvadurai and Glaser, 2017; Ke et al., 2018). The participation of the dominant asperities in the nucleation of larger events (Fig. 3) suggests that perhaps the hierarchical ruptures observed in nature occur on worn asperities that potentially act as "kicks" to a rate-dependent cascade model (Noda et al., 2013; McLaskey, 2019).

6.4. Effect of relative toughness of the fault on nucleation

At lower levels of relative toughness between the smooth and rough regions, nucleation occurred in a smooth manner, following the preslip model. We believe that this can be explained as the critical nucleation length for the rough regions ($L_{c,high}$), which is on the order of size of the dominant asperity L_{A1} (Fig. 3(a)). In this case, the size of the expanding preslip region was $L_{c,high} \approx L_{A1}$ and nucleation could occur smoothly from an instability that nucleated on a small smooth patch within $A1$. Since the tough barriers within the dominant $A1$ asperity were generally weaker at lower relative toughness level, this leads to smooth, uninhibited growth into the nucleation of a large mainshock.

As the toughness was increased, two mechanisms were observed. Firstly, the perturbations from the foreshocks generated on dominant asperities became more easily constrained/arrested. Secondly, the critical length scale of the rough region was now larger than the length of the $A1$ asperity ($L_{c,high} > L_{A1}$). This meant that the size of the preslip region L_{pre} had to surpass the size of the dominant asperity (just slightly) to achieve nucleation of a larger rupture. During the slow expansion of preslip beyond the dominant asperity length scale, the brittle patches were generating seismicity that contributed to the growth of the preslip zone in the tougher region. Once at a critical state, i.e. the size of the preslip region was almost the size of the nucleation length for the rough barrier, the next foreshock would "kick" the system sufficiently to initiate the nucleation of a mainshock.

7. Conclusions

We implemented frictional heterogeneity into numerical simulations to capture slow aseismic transients coupled with localized foreshocks and compared this to the observed behavior in laboratory experiments on a fault analog. Our model prescribed RSF frictional properties based on the worn surface roughness that displayed a bimodal Gaussian distribution of surface heights. This was done by segmenting the smooth and rough faults into a "barcode-style" representation of friction. We found that this discretization produced dominant asperities that were prone to seismicity throughout the simulations.

The numerical models produced a rich behavior of seismicity; the dominant asperities progressively weakened the fault during the interseismic period. This was followed by their direct participation in the acceleration of the nucleation sequence of larger ruptures. Foreshocks

from the dominant asperities produced higher accelerations rates as the surrounding fault toughness (i.e. fracture energy) was increased. We found these asperities produced a *rate-dependent cascade model* that is a combination of the debated preslip and cascading model.

We validated the results using two methods: (*1*) The source properties from the localized ruptures in our model were comparable to independent kinematic estimates made by Selvadurai (2019). (*2*) The slow rupture expansion rate between seismic features on the dominant asperities and the accelerated creep prior to nucleation matched those observed in similar experiments by Selvadurai et al. (2017) and slow slip event in nature (e.g. Passarelli et al., 2021).

Heterogeneity of frictional properties on natural faults relies on the inherent discreteness since this acts as a tuning parameter to match fault dynamics. Natural features on faults, such as fault mirrors, have only recently been explained in the literature and are becoming more prevalent, reproducible and observable in the laboratory. While more research will be needed in both laboratory experiments and the study of fault outcrops, our model may provide a physical mechanism to a specific component of hierarchical structures that may be responsible for repeating hierarchical sequences of earthquakes in nature.

CRediT authorship contribution statement

P.A. Selvadurai: Conceptualization, Methodology, Software, Formal-analysis, Data-curation, Writing-original-draft, Writing-review-editing, Visualization. **P. Galvez:** Methodology, Software, Data-curation. **P.M. Mai:** Funding-acquisition, Supervision, Methodology, Writing-review-editing. **S.D. Glaser:** Funding-acquisition.

Declaration of Competing Interest

The authors declare the following financial interests/personal relationships which may be considered as potential competing interests: Paul Selvadurai reports financial support was provided by ETH Zurich. Paul Selvadurai reports financial support was provided by JSPS KAKENHI Grant No. JP16H06478. Percy Galvez, Martin Mai reports financial support was provided by Information Technology Division and Extreme Computing Research Center (ECRC) at KAUST. Steven D. Glaser reports financial support was provided by National Science Foundation Grant CMMI-1131582.

Data availability

Data will be made available on request.

Acknowledgments

We would like to thank T. Yamaguchi who provided important discussion points regarding the analysis, three anonymous reviewers and thoughtful comments from P. Romanet. Key insights into simulations presented here are given by J.-P. Ampuero. This research was supported by: JSPS KAKENHI Grant No. JP16H06478 in Scientific Research on Innovative Areas “Science of Slow Earthquakes”. Computational resources were provided by the Information Technology Division and Extreme Computing Research Center (ECRC) at KAUST. Funding for parts of this research was provided by the National Science Foundation Grant CMMI-1131582 awarded to SDG at the University of California, Berkeley. Partial funding for PAS was provided from the European Research Council (ERC) project FEAR (grant 856559) under the European Community’s Horizon 2020 Framework Programme. PMM’s contribution to this study and a research visit of PAS to KAUST was supported by KAUST research grant BAS/1/1339–01-01. The authors assume full responsibility for the comments and concepts presented in the paper. All data sets required to reproduce the results presented here are freely available at this site (doi.org/10.3929/ethz-b-000405620). Please contact the corresponding author for access.

Appendix A. Supplementary data

Supplementary data to this article can be found online at https://doi.org/10.1016/j.tecto.2022.229689.

References

Adachi, K., Kato, K., 2000. Formation of smooth wear surfaces on alumina ceramics by embedding and tribo-sintering of fine wear particles. Wear 245, 84–91. https://doi.org/10.1016/S0043-1648(00)00468-3. URL:http://www.sciencedirect.com/science/article/pii/S0043164800004683.

Aochi, H., Ide, S., 2014. Ground motions characterized by a multi-scale heterogeneous earthquake model. Earth Planets Space 66.

Aochi, H., Ide, S., 2017. Role of multiscale heterogeneity in fault slip from quasi-static numerical simulations. Earth Planets Space 69, 94. https://doi.org/10.1186/s40623-017-0676-5.

Barbot, S., Lapusta, N., Avouac, J., 2012. Under the Hood of the Earthquake Machine: Toward Predictive Modeling of the Seismic Cycle. Science 336, 707–710. https://doi.org/10.1126/science.1218796. URL:http://www.sciencemag.org/content/336/6082/707.abstract, arXiv:http://www.sciencemag.org/content/336/6082/707.full.pdf.

Bartlow, N.M., Miyazaki, S., Bradley, A.M., Segall, P., 2011. Space-time correlation of slip and tremor during the 2009 Cascadia slow slip event. Geophys. Res. Lett. 38, l18309 https://doi.org/10.1029/2011GL048714 n/a–n/a.

Baumberger, T., Caroli, C., 2006. Solid friction from stick-slip down to pinning and aging. Adv. Phys. 55, 279–348. https://doi.org/10.1080/00018730600732186.

Ben-Zion, Y., Rice, J.R., 1995. Slip patterns and earthquake populations along different classes of faults in elastic solids. J. Geophys. Res. 100, 12959–12983. https://doi.org/10.1029/94jb03037.

Beroza, G.C., Ellsworth, W.L., 1996. Properties of the seismic nucleation phase. Tectonophysics 261, 209–227. https://doi.org/10.1016/0040-1951(96)00067-4.

Berthoude, P., Baumberger, T., G’Sell, C., Hiver, J.M., 1999. Physical analysis of the state- and rate-dependent friction law: Static friction. Phys. Rev. B: Condens. Matter Mater. Phys. 59, 14313–14327. https://doi.org/10.1103/PhysRevB.59.14313.

Borucki, L.J., 2002. Mathematical modeling of polish-rate decay in chemical-mechanical polishing. J. Eng. Math. 43, 105–114. https://doi.org/10.1023/A:1020305108358.

Borucki, L.J., Witelski, T., Please, C., Kramer, P.R., Schwendeman, D., 2004. A theory of pad conditioning for chemical-mechanical polishing. J. Eng. Math. 50, 1–24. https://doi.org/10.1023/B:ENGI.0000042116.09084.00.

Bouchon, M., Karabulut, H., Aktar, M., Ozalaybey, S., Schmittbuhl, J., Bouin, M.P., 2011. Extended nucleation of the 1999 M_w 7.6 Izmit earthquake. Science 331, 877–880. https://doi.org/10.1126/science.1197341.

Brodsky, E.E., Lay, T., 2014. Recognizing Foreshocks from the 1 April 2014 Chile Earthquake. Science 344, 700–702. https://doi.org/10.1126/science.1255202.

Brune, J.N., 1970. Tectonic stress and spectra of seismic shear waves from earthquakes. J. Geophys. Res. 75, 4997–5009. https://doi.org/10.1029/JB075i026p04997.

Buijze, L., Guo, Y., Niemeijer, A.R., Ma, S., Spiers, C.J., 2020. Nucleation of stick-slip instability within a large-scale experimental fault: effects of stress heterogeneities due to loading and gouge-layer compaction. J. Geophys. Res.: Solid Earth n/a, e2019JB018429. https://doi.org/10.1029/2019JB018429. URL:https://agupubs.onlinelibrary.wiley.com/doi/abs/10.1029/2019JB018429.

Bürgmann, R., 2014. Warning signs of the Iquique earthquake. Nature 512, 258–259.

Castellano, M., Lorez, F., Kammer, D., 2023. Nucleation of frictional slip: A yielding or a fracture process? Accepted in J. Mech. Phys. Solids. https://doi.org/10.48550/ARXIV.2209.07814. https://arxiv.org/abs/2209.07814.

Cattania, C., Segall, P., 2019. Crack Models of Repeating Earthquakes Predict Observed Moment-Recurrence Scaling. J. Geophys. Res.: Solid Earth 124, 476–503. https://doi.org/10.1029/2018JB016056. URL:https://agupubs.onlinelibrary.wiley.com/doi/abs/10.1029/2018JB016056, arXiv:https://agupubs.onlinelibrary.wiley.com/doi/pdf/10.1029/2018JB016056.

Cattania, C., Segall, P., 2021. Precursory Slow Slip and Foreshocks on Rough Faults. J. Geophys. Res.: Solid Earth 126, e2020JB020430. https://doi.org/10.1029/2020JB020430. URL:https://agupubs.onlinelibrary.wiley.com/doi/abs/10.1029/2020JB020430, arXiv:https://agupubs.onlinelibrary.wiley.com/doi/pdf/10.1029/2020JB020430. e2020JB020430 2020JB020430.

Chen, T., Lapusta, N., 2009. Scaling of small repeating earthquakes explained by interaction of seismic and aseismic slip in a rate and state fault model. J. Geophys. Res.: Solid Earth 114. https://doi.org/10.1029/2008JB005749. URL:https://agupubs.onlinelibrary.wiley.com/doi/abs/10.1029/2008JB005749, arXiv:https://agupubs.onlinelibrary.wiley.com/doi/pdf/10.1029/2008JB005749.

Cocco, M., Aretusini, S., Cornelio, C., Neilsen, S., Spagnuolo, E., Tinti, E., Di Toro, G., 2023. Fracture energy and breakdown work during earthquakes. Ann. Rev. Earth Planet. Sci. https://doi.org/10.1146/annurev-earth-071822-100304.

Cornelio, C., Spagnuolo, E., Aretusini, S., Nielsen, S., Passelègue, F., Violay, M., Cocco, M., Di Toro, G., 2022. Determination of Parameters Characteristic of Dynamic Weakening Mechanisms During Seismic Faulting in Cohesive Rocks. J. Geophys. Res.: Solid Earth 127, e2022JB024356. https://doi.org/10.1029/2022JB024356. URL:https://agupubs.onlinelibrary.wiley.com/doi/abs/10.1029/2022JB024356, arXiv:https://agupubs.onlinelibrary.wiley.com/doi/pdf/10.1029/2022JB024356. e2022JB024356 2022JB024356.

Dal Zilio, L., Lapusta, N., Avouac, J.P., 2020. Unraveling Scaling Properties of Slow-Slip Events. Geophys. Res. Lett. 47, e2020GL087477 https://doi.org/10.1029/2020GL087477. URL:https://agupubs.onlinelibrary.wiley.com/doi/abs/10.1029/2

020GL087477, arXiv:https://agupubs.onlinelibrary.wiley.com/doi/pdf/10.1029/2020GL087477. e2020GL087477 10.1029/2020GL087477.
Dieterich, J.H., 1978. Preseismic fault slip and earthquake prediction. J. Geophys. Res. 83, 3940–3948. https://doi.org/10.1029/JB083iB08p03940.
Dieterich, J.H., 1979. Modeling of rock friction: 1. Experimental results and constitutive equations. J. Geophys. Res. 84, 2161–2168. https://doi.org/10.1029/JB084iB05p02161.
Dieterich, J.H., 1992. Earthquake nucleation on faults with rate-and state-dependent strength. Tectonophysics 211, 115–134. https://doi.org/10.1016/0040-1951(92)90055-B. URL:http://www.sciencedirect.com/science/article/pii/004019519290055B.
Dieterich, J.H., Kilgore, B.D., 1994. Direct observation of frictional contacts: New insights for state-dependent properties. Pure Appl. Geophys. 143, 283–302. https://doi.org/10.1007/BF00874332.
Dieterich, J.H., Richards-Dinger, K.B., 2010. Earthquake recurrence in simulated fault systems. Pure Appl. Geophys. 167, 1087–1104. https://doi.org/10.1007/s00024-010-0094-0.
Dodge, D.A., Beroza, G.C., Ellsworth, W.L., 1995. Foreshock sequence of the 1992 Landers, California, earthquake and its implications for earthquake nucleation. J. Geophys. Res. 100, 9865–9880. https://doi.org/10.1029/95JB00871.
Ellsworth, W.L., Beroza, G.C., 1995. Seismic evidence for an earthquake nucleation phase. Science 268, 851–855. https://doi.org/10.1126/science.268.5212.851.
Ellsworth, W.L., Bulut, F., 2018. Nucleation of the 1999 izmit earthquake by a triggered cascade of foreshocks. Nat. Geosci. 11, 531–535. https://doi.org/10.1038/s41561-018-0145-1.
Erickson, B.A., Jiang, J., Barall, M., Lapusta, N., Dunham, E.M., Harris, R., Abrahams, L. S., Allison, K.L., Ampuero, J., Barbot, S., Cattania, C., Elbanna, A., Fialko, Y., Idini, B., Kozdon, J.E., Lambert, V., Liu, Y., Luo, Y., Ma, X., Best McKay, M., Segall, P., Shi, P., van den Ende, M., Wei, M., 2020. The Community Code Verification Exercise for Simulating Sequences of Earthquakes and Aseismic Slip (SEAS). Seismol. Res. Lett. 91, 874–890. https://doi.org/10.1785/0220190248. URL:https://doi.org/10.1785/0220190248, arXiv:https://pubs.geoscienceworld.org/ssa/srl/article-pdf/91/2A/874/4956491/srl-2019248.1.pdf.
Fan, Y., Gu, F., Ball, A., 2010. Modelling acoustic emissions generated by sliding friction. Wear 268, 811–815. URL:http://www.sciencedirect.com/science/article/pii/S0043164809006322.
Fondriest, M., Smith, S., Candela, T., Nielsen, S.B., Mair, K., Di Toro, G., 2013. Mirror-like faults and power dissipation during earthquakes. Geology 41, 1175–1178. https://doi.org/10.1130/G34641.1. URL: arXiv:https://pubs.geoscienceworld.org/geology/article-pdf/41/11/1175/3543066/1175.pdf.
Fukuyama, E., Tsuchida, K., Kawakata, H., Yamashita, F., Mizoguchi, K., Xu, S., 2018. Spatiotemporal complexity of 2-D rupture nucleation process observed by direct monitoring during large-scale biaxial rock friction experiments. Tectonophysics 733, 182–192. https://doi.org/10.1016/j.tecto.2017.12.023. URL:http://www.sciencedirect.com/science/article/pii/S0040195117305267. physics of Earthquake Rupture Propagation.
Goldberg, R., Siman-Tov, S., Emmanuel, S., 2016. Weathering resistance of carbonate fault mirrors promotes rupture localization. Geophys. Res. Lett. 43, 3105–3111. https://doi.org/10.1002/2016GL067788, 2016GL067788.
Gomberg, J., 2018. Unsettled earthquake nucleation. Nat. Geosci. 11, 463–464. https://doi.org/10.1038/s41561-018-0149-x.
He, D., Zhou, P., Yan, Y., Kang, R., Guo, D., 2017. Nonlinear Compression Behavior of the Grooved Polishing Pad: A Model and Its Validation. ECS J. Solid State Sci. Technol. 6, 178–183.
Heimisson, E.R., 2020. Crack to pulse transition and magnitude statistics during earthquake cycles on a self-similar rough fault. Earth Planet. Sci. Lett. 537, 116202 https://doi.org/10.1016/j.epsl.2020.116202. URL:https://www.sciencedirect.com/science/article/pii/S0012821X2030145X.
Hillers, G., Ben-Zion, Y., Mai, P.M., 2006. Seismicity on a fault controlled by rate- and state-dependent friction with spatial variations of the critical slip distance. J. Geophys. Res. 111 https://doi.org/10.1029/2005jb003859.
Hillers, G., Mai, P.M., Ben-Zion, Y., Ampuero, J.P., 2007. Statistical properties of seismicity of fault zones at different evolutionary stages. Geophys. J. Int. 169, 515–533. https://doi.org/10.1111/j.1365-246X.2006.03275.x arXiv:https://academic.oup.com/gji/article-pdf/169/2/515/5905493/169-2-515.pdf.
Horowitz, F.G., Ruina, A., 1989. Slip patterns in a spatially homogeneous fault model. J. Geophys. Res.: Solid Earth 94, 10279–10298. https://doi.org/10.1029/JB094iB08p10279. URL:https://agupubs.onlinelibrary.wiley.com/doi/abs/10.1029/JB094iB08p10279, arXiv:https://agupubs.onlinelibrary.wiley.com/doi/pdf/10.1029/JB094iB08p10279.
Hu, S., Huang, W., Shi, X., Peng, Z., Liu, X., 2019. Bi-fractal feature of bi-Gaussian stratified surfaces. Tribol. Int. 134, 427–434. URL:http://www.sciencedirect.com/science/article/pii/S0301679X19300854.
Hu, S., Huang, W., Shi, X., Peng, Z., Liu, X., 2019. Mechanism of bi-gaussian surface topographies on generating acoustic emissions under a sliding friction. Tribol. Int. 131, 64–72. URL:http://www.sciencedirect.com/science/article/pii/S0301679X18304961.
Ide, S., 2019. Frequent observations of identical onsets of large and small earthquakes. Nature 573, 112–116.
Ide, S., Aochi, H., 2005. Earthquakes as multiscale dynamic ruptures with heterogeneous fracture surface energy. J. Geophys. Res.: Solid Earth 110. https://doi.org/10.1029/2004JB003591 n/a–n/a.
Johnson, K.L., 1985. Contact Mechanics. Cambridge University Press.
Kaneko, Y., Ampuero, J.P., 2011. A mechanism for preseismic steady rupture fronts observed in laboratory experiments. Geophys. Res. Lett. 38 https://doi.org/10.1029/2011GL049953 arXiv:https://agupubs.onlinelibrary.wiley.com/doi/pdf/10.1029/2011GL049953.
Kaneko, Y., Avouac, J.P., Lapusta, N., 2010. Towards inferring earthquake patterns from geodetic observations of interseismic coupling. Nat. Geosci. 3, 363–369. https://doi.org/10.1038/ngeo843.
Kaneko, Y., Nielsen, S.B., Carpenter, B.M., 2016. The onset of laboratory earthquakes explained by nucleating rupture on a rate-and-state fault. J. Geophys. Res.: Solid Earth 121, 6071–6091. https://doi.org/10.1002/2016JB013143 arXiv:https://agupubs.onlinelibrary.wiley.com/doi/pdf/10.1002/2016JB013143.
Kato, A., Fukuda, J., Kumazawa, T., Nakagawa, S., 2016. Accelerated nucleation of the 2014 Iquique, Chile Mw 8.2 Earthquake. Sci. Rep. 6 https://doi.org/10.1038/srep24792.
Kato, A., Obara, K., Igarashi, T., Hiroshi, T., Nakagawa, S., Hirata, N., 2012. Propagation of Slow Slip Leading Up to the 2011 Mw 9.0 Tohoku-Oki Earthquake. Science 335, 705–708.
Kato, N., 2003. Repeating Slip Events at a Circular Asperity: Numerical Simulation with a Rate- and State-Dependent Friction Law. Bull. Earthq. Res. Inst. Univ. Tokyo 78, 151–166.
Ke, C.Y., McLaskey, G.C., Kammer, D.S., 2018. Rupture Termination in Laboratory-Generated Earthquakes. Geophys. Res. Lett. 45, 12784–12792. https://doi.org/10.1029/2018GL080492 arXiv:https://agupubs.onlinelibrary.wiley.com/doi/pdf/10.1029/2018GL080492.
Kirkpatrick, J.D., Rowe, C.D., White, J.C., Brodsky, E.E., 2013. Silica gel formation during fault slip: Evidence from the rock record. Geology 41, 1015–1018. https://doi.org/10.1130/G34483.1.
Köpfli, M., Gräff, D., Lipovsky, B.P., Selvadurai, P.A., Farinotti, D., Walter, F., 2022. Hydraulic Conditions for Stick-Slip Tremor Beneath an Alpine Glacier. Geophys. Res. Lett. 49, e2022GL100286 https://doi.org/10.1029/2022GL100286.
Kroll, K.A., Richards-Dinger, K.B., Dieterich, J.H., 2017. Sensitivity of Induced Seismic Sequences to Rate-and-State Frictional Processes. J. Geophys. Res.: Solid Earth 122, 10207–10219. https://doi.org/10.1002/2017JB014841. URL:https://agupubs.onlinelibrary.wiley.com/doi/abs/10.1002/2017JB014841, arXiv:https://agupubs.onlinelibrary.wiley.com/doi/pdf/10.1002/2017JB014841.
Lapusta, N., Rice, J.R., 2003. Nucleation and early seismic propagation of small and large events in a crustal earthquake model. J. Geophys. Res. 108 https://doi.org/10.1029/2001jb000793.
Latour, S., Schubnel, A., Nielsen, S., Madariaga, R., Vinciguerra, S., 2013. Characterization of nucleation during laboratory earthquakes. Geophys. Res. Lett. 40, 5064–5069. https://doi.org/10.1002/grl.50974.
Leefe, S.E., Dowson, D., Taylor, C.M., Childs, T.H.C., Dalmaz, G., Berthier, Y., Flamand, L., Georges, J.M., Lubrecht, A.A., 1998. "Bi-Gaussian" representation of worn surface topography in elastic contact problems. In: Tribology Series, vol. 34. Elsevier, pp. 281–290. URL:http://www.sciencedirect.com/science/article/pii/S0167892298800837.
Lipovsky, B.P., Dunham, E.M., 2017. Slow-slip events on the Whillans Ice Plain, Antarctica, described using rate-and-state friction as an ice stream sliding law. J. Geophys. Res.: Earth Surf. 122, 973–1003. https://doi.org/10.1002/2016JF004183. URL:https://agupubs.onlinelibrary.wiley.com/doi/abs/10.1002/2016JF004183, arXiv:https://agupubs.onlinelibrary.wiley.com/doi/pdf/10.1002/2016JF004183.
Liu, Y., Rice, J.R., 2007. Spontaneous and triggered aseismic deformation transients in a subduction fault model. J. Geophys. Res.: Solid Earth 112. https://doi.org/10.1029/2007JB004930. URL:https://agupubs.onlinelibrary.wiley.com/doi/abs/10.1029/2007JB004930, arXiv:https://agupubs.onlinelibrary.wiley.com/doi/pdf/10.1029/2007JB004930.
Liu, Y., Rice, J.R., 2005. Aseismic slip transients emerge spontaneously in three-dimensional rate and state modeling of subduction earthquake sequences. J. Geophys. Res. 110 https://doi.org/10.1029/2004jb003424.
Luo, Y., Ampuero, J.P., Galvez, P., van den Ende, M., Idini, B., 2017a. QDYN: a Quasi-DYNamic earthquake simulator (v1.1). doi:10.5281/zenodo.322459.
Luo, Y., Ampuero, J.P., Miyakoshi, K., Irikura, K., 2017b. Surface Rupture Effects on Earthquake Moment-Area Scaling Relations. Pure Appl. Geophys. 174, 3331–3342. https://doi.org/10.1007/s00024-017-1467-4.
Ma, S., Ma, J., Liu, L., 2002. Experimental evidence for seismic nucleation phase. Chin. Sci. Bull. 47, 769–773. https://doi.org/10.1360/02tb9174.
Maegawa, S., Suzuki, A., Nakano, K., 2010. Precursors of Global Slip in a Longitudinal Line Contact Under Non-Uniform Normal Loading. Tribol. Lett. 38, 313–323. https://doi.org/10.1007/s11249-010-9611-7.
Marone, C., Cox, S.J.D., 1994. Scaling of rock friction constitutive parameters: The effects of surface roughness and cumulative offset on friction of gabbro. Pure Appl. Geophys. 143, 359–385. https://doi.org/10.1007/BF00874335.
McLaskey, G.C., 2019. Earthquake Initiation From Laboratory Observations and Implications for Foreshocks. J. Geophys. Res.: Solid Earth 124, 12882–12904. https://doi.org/10.1029/2019JB018363. URL:https://agupubs.onlinelibrary.wiley.com/doi/abs/10.1029/2019JB018363, arXiv:https://agupubs.onlinelibrary.wiley.com/doi/pdf/10.1029/2019JB018363.
McLaskey, G.C., Kilgore, B.D., 2013. Foreshocks during the nucleation of stick-slip instability. J. Geophys. Res. 118, 2982–2997. https://doi.org/10.1002/jgrb.50232.
McLaskey, G.C., Kilgore, B.D., Lockner, D.A., Beeler, N.M., 2014. Laboratory Generated M -6 Earthquakes. Pure Appl. Geophys. https://doi.org/10.1007/s00024-013-0772-9.
McLaskey, G.C., Lockner, D.A., 2014. Preslip and cascade processes initiating laboratory stick slip. J. Geophys. Res.: Solid Earth 119, 6323–6336. https://doi.org/10.1002/2014JB011220.
Mignan, A., 2014. The debate on the prognostic value of earthquake foreshocks: A meta-analysis. Sci. Rep. 4, 4099.

Mignan, A., 2020. Asymmetric Laplace Mixture Modelling of Incomplete Power-Law Distributions: Application to 'Seismicity Vision'. In: Arai, K., Kapoor, S. (Eds.), Advances in Computer Vision. Springer International Publishing, Cham, pp. 30–43.
Nielsen, S., Taddeucci, J., Vinciguerra, S., 2010. Experimental observation of stick-slip instability fronts. Geophys. J. Int. 180, 697–702. https://doi.org/10.1111/j.1365-246X.2009.04444.x.
Noda, H., Nakatani, M., Hori, T., 2013. Large nucleation before large earthquakes is sometimes skipped due to cascade-up – Implications from a rate and state simulation of faults with hierarchical asperities. J. Geophys. Res.: Solid Earth 118, 2924–2952. https://doi.org/10.1002/jgrb.50211. URL:https://agupubs.onlinelibrary.wiley.com/doi/abs/10.1002/jgrb.50211, arXiv:https://agupubs.onlinelibrary.wiley.com/doi/pdf/10.1002/jgrb.50211.
Obara, K., Kato, A., 2016. Connecting slow earthquakes to huge earthquakes. Science 353, 253–257. https://doi.org/10.1126/science.aaf1512 arXiv:http://science.sciencemag.org/content/353/6296/253.full.pdf.
Ohnaka, M., 1992. Earthquake source nucleation: A physical model for short-term precursors. Tectonophysics 211, 149–178. https://doi.org/10.1016/0040-1951(92)90057-D.
Ohnaka, M., 1993. Critical Size of the Nucleation Zone of Earthquake Rupture Inferred from Immediate Foreshock Activity. J. Phys. Earth 41, 45–56. https://doi.org/10.4294/jpe1952.41.45.
Ohnaka, M., Shen, L.F., 1999. Scaling of the shear rupture process from nucleation to dynamic propagation: Implications of geometric irregularity of the rupturing surfaces. J. Geophys. Res. 104, 817–844. https://doi.org/10.1029/1998JB900007.
Ohnaka, M., Yamashita, T., 1989. A cohesive zone model for dynamic shear faulting based on experimentally inferred constitutive relation and strong motion source parameters. J. Geophys. Res.: Solid Earth 94, 4089–4104. https://doi.org/10.1029/JB094iB04p04089. URL:https://agupubs.onlinelibrary.wiley.com/doi/abs/10.1029/JB094iB04p04089, arXiv:https://agupubs.onlinelibrary.wiley.com/doi/pdf/10.1029/JB094iB04p04089.
Okubo, P.G., Dieterich, J.H., 1984. Effects of physical fault properties on frictional instabilities produced on simulated faults. J. Geophys. Res. 89, 5817–5827. https://doi.org/10.1029/JB089iB07p05817.
Okuda, T., Ide, S., 2018. Hierarchical rupture growth evidenced by the initial seismic waveforms. Nat. Commun. 9.
Okuda, T., Ide, S., 2018. Streak and hierarchical structures of the Tohoku-Hokkaido subduction zone plate boundary. Earth Planets Space 70, 132. https://doi.org/10.1186/s40623-018-0903-8.
Ozawa, S., Ando, R., 2021. Mainshock and Aftershock Sequence Simulation in Geometrically Complex Fault Zones. J. Geophys. Res.: Solid Earth 126, e2020JB020865. https://doi.org/10.1029/2020JB020865. URL:https://agupubs.onlinelibrary.wiley.com/doi/abs/10.1029/2020JB020865, arXiv:https://agupubs.onlinelibrary.wiley.com/doi/pdf/10.1029/2020JB020865. e2020JB020865 2020JB020865.
Ozawa, S.W., Hatano, T., Kame, N., 2019. Longer Migration and Spontaneous Decay of Aseismic Slip Pulse Caused by Fault Roughness. Geophys. Res. Lett. 46, 636–643. https://doi.org/10.1029/2018GL081465.
Passarelli, L., Selvadurai, P.A., Rivalta, E., Jónsson, S., 2021. The source scaling and seismic productivity of slow slip transients. Sci. Adv. 7 https://doi.org/10.1126/sciadv.abg9718.
Passelègue, F.X., Latour, S., Schubnel, A., Nielsen, S., Bhat, H.S., Madariaga, R., 2017. Influence of Fault Strength on Precursory Processes During Laboratory Earthquakes. American Geophysical Union (AGU). https://doi.org/10.1002/9781119156895.ch12, pp. 229–242. Chapter 12. URL:https://agupubs.onlinelibrary.wiley.com/doi/abs/10.1002/9781119156895.ch12, arXiv:https://agupubs.onlinelibrary.wiley.com/doi/pdf/10.1002/9781119156895.ch12.
Pawlus, P., 2008. Simulation of stratified surface topographies. Wear 264, 457–463. URL:http://www.sciencedirect.com/science/article/pii/S0043164807002062.
Pluymakers, A., Røyne, A., 2017. Nanograin formation and reaction-induced fracturing due to decarbonation: Implications for the microstructures of fault mirrors. Earth Planet. Sci. Lett. 476, 59–68. URL:http://www.sciencedirect.com/science/article/pii/S0012821X17304387.
Pozzi, G., De Paola, N., Nielsen, S.B., Holdsworth, R.E., Bowen, L., 2018. A new interpretation for the nature and significance of mirror-like surfaces in experimental carbonate-hosted seismic faults. Geology 46, 583. https://doi.org/10.1130/G40197.1.
Rabinowicz, E., 1956. Autocorrelation analysis of the sliding process. J. Appl. Phys. 27, 131–135. https://doi.org/10.1063/1.1722321.
Ranjith, K., Rice, J.R., 1999. Stability of quasi-static slip in a single degree of freedom elastic system with rate and state dependent friction. J. Mech. Phys. Solids 47, 1207–1218. https://doi.org/10.1016/S0022-5096(98)00113-6. URL:http://www.sciencedirect.com/science/article/pii/S0022509698001136.
Rice, J.R., 1993. Spatio-temporal complexity of slip on a fault. J. Geophys. Res.: Solid Earth 98, 9885–9907. https://doi.org/10.1029/93JB00191 arXiv:https://agupubs.onlinelibrary.wiley.com/doi/pdf/10.1029/93JB00191.
Ripperger, J., Ampuero, J.P., Mai, P.M., Giardini, D., 2007. Earthquake source characteristics from dynamic rupture with constrained stochastic fault stress. J. Geophys. Res. 112, B04311. https://doi.org/10.1029/2006JB004515.
Roeloffs, E.A., 2006. Evidence for aseismic deformation rate changes prior to earthquakes. Annu. Rev. Earth Planet. Sci. 34, 591–627. https://doi.org/10.1146/annurev.earth.34.031405.124947. URL:https://doi.org/10.1146/annurev.earth.34.031405.124947, arXiv:https://doi.org/10.1146/annurev.earth.34.031405.124947.
Romanet, P., Bhat, H.S., Jolivet, R., Madariaga, R., 2018. Fast and Slow Slip Events Emerge Due to Fault Geometrical Complexity. Geophys. Res. Lett. 45, 4809–4819. https://doi.org/10.1029/2018GL077579. URL:https://agupubs.onlinelibrary.wiley.com/doi/abs/10.1029/2018GL077579, arXiv:https://agupubs.onlinelibrary.wiley.com/doi/pdf/10.1029/2018GL077579.
Rubin, A.M., Ampuero, J.P., 2005. Earthquake nucleation on (aging) rate and state faults. J. Geophys. Res.: Solid Earth 110. https://doi.org/10.1029/2005JB003686 n/a–n/a.
Rubinstein, S.M., Cohen, G., Fineberg, J., 2004. Detachment fronts and the onset of dynamic friction. Nature 430, 1005–1009. https://doi.org/10.1038/nature02830.
Ruina, A., 1983. Slip instability and state variable friction laws. J. Geophys. Res. 88, 10359–10370. https://doi.org/10.1029/JB088iB12p10359.
Schmittbuhl, J., Chambon, G., Hansen, A., Bouchon, M., 2006. Are stress distributions along faults the signature of asperity squeeze? Geophys. Res. Lett. 33, L13307.
Scholz, C.H., Aviles, C.A., 1986. The Fractal Geometry of Faults and Faulting. American Geophysical Union (AGU). https://doi.org/10.1029/GM037p0147, pp. 147–155, arXiv:https://agupubs.onlinelibrary.wiley.com/doi/pdf/10.1029/GM037p0147.
Segall, P., Rice, J.R., 1995. Dilatancy, compaction, and slip instability of a fluid-infiltrated fault. J. Geophys. Res. 100, 22155–22171. https://doi.org/10.1029/95JB02403.
Seif, S., Zechar, J.D., Mignan, A., Nandan, S., Wiemer, S., 2018. Foreshocks and Their Potential Deviation from General Seismicity. Bull. Seismol. Soc. Am. 109, 1–18. https://doi.org/10.1785/0120170188.
Selvadurai, P.A., 2019. Laboratory insight into seismic estimates of energy partitioning during dynamic rupture: An observable scaling breakdown. J. Geophys. Res.: Solid Earth.
Selvadurai, P.A., Glaser, S.D., 2015. Laboratory-developed Contact Models Controlling Instability on Frictional Faults. J. Geophys. Res. 120, 4208–4236. https://doi.org/10.1002/2014JB011690.
Selvadurai, P.A., Glaser, S.D., 2015. Novel Monitoring Techniques for Characterizing Frictional Interfaces in the Laboratory. Sensors 15, 9791–9814. https://doi.org/10.3390/s150509791.
Selvadurai, P.A., Glaser, S.D., 2017. Asperity generation and its relationship to seismicity on a planar fault: A laboratory simulation. Geophys. J. Int. 208, 1009–1025. https://doi.org/10.1093/gji/ggw439.
Selvadurai, P.A., Glaser, S.D., Parker, J.M., 2017. On factors controlling precursor slip fronts in the laboratory and their relation to slow slip events in nature. Geophys. Res. Lett. 44 https://doi.org/10.1002/2017GL072538.
Shi, Q., Barbot, S., Wei, S., Tapponnier, P., Matsuzawa, T., Shibazaki, B., 2020. Structural control and system-level behavior of the seismic cycle at the Nankai Trough. Earth Planets Space 72, 27. https://doi.org/10.1186/s40623-020-1145-0.
Siman-Tov, S., Aharonov, E., Boneh, Y., Reches, Z., 2015. Fault mirrors along carbonate faults: Formation and destruction during shear experiments. Earth Planet. Sci. Lett. 430, 367–376. https://doi.org/10.1016/j.epsl.2015.08.031. URL:http://www.sciencedirect.com/science/article/pii/S0012821X15005579.
Siman-Tov, S., Aharonov, E., Sagy, A., Emmanuel, S., 2013. Nanograins form carbonate fault mirrors. Geology 41, 703–706.
Siman-Tov, S., Stock, G.M., Brodsky, E.E., White, J.C., 2017. The coating layer of glacial polish. Geology 45, 987–990. https://doi.org/10.1130/G39281.1.
Tal, Y., Hager, B.H., Ampuero, J.P., 2018. The Effects of Fault Roughness on the Earthquake Nucleation Process. J. Geophys. Res.: Solid Earth 123, 437–456. https://doi.org/10.1002/2017JB014746.
Tisato, N., Di Toro, G., De Rossi, N., Quaresimin, M., Candela, T., 2012. Experimental investigation of flash weakening in limestone. J. Struct. Geol. 38, 183–199. https://doi.org/10.1016/j.jsg.2011.11.017. URL:http://www.sciencedirect.com/science/article/pii/S0191814111002057. Physico-Chemical Processes in Seismic Faults.
Tse, S.T., Rice, J.R., 1986. Crustal earthquake instability in relation to the depth variation of frictional slip properties. J. Geophys. Res. 91, 9452–9472. https://doi.org/10.1029/jb091ib09p09452.
Wang, K., Bilek, S.L., 2014. Invited review paper: Fault creep caused by subduction of rough seafloor relief. Tectonophysics 610, 1–24. URL:http://www.sciencedirect.com/science/article/pii/S0040195113006896.
Wiemer, S., Wyss, M., 2002. Mapping spatial variability of the frequency-magnitude distribution of earthquakes. In: Adv. Geophys., vol. 45. Elsevier. https://doi.org/10.1016/S0065-2687(02)80007-3, pp. 259–V. URL:http://www.sciencedirect.com/science/article/pii/S0065268702800073.
Xu, S., Fukuyama, E., Yamashita, F., 2019. Robust estimation of rupture properties at propagating front of laboratory earthquakes. J. Geophys. Res. Solid Earth 124, 766–787. https://doi.org/10.1029/2018JB016797.
Yamashita, F., Fukuyama, E., Xu, S., Kawakata, H., Mizoguchi, K., Takizawa, S., 2021. Two end-member earthquake preparations illuminated by foreshock activity on a meter-scale laboratory fault. Nat. Commun. 12, 4302. https://doi.org/10.1038/s41467-021-24625-4.
Yin, Y., Galvez, P., Heimisson, E.R., Wiemer, S., 2022. The role of three-dimensional fault interactions in creating complex seismic sequences and power-law magnitude distributions. Earth Space Sci. Open Arch. 18 https://doi.org/10.1002/essoar.10510908.1.
Yoshioka, N., 1997. A review of the micromechanical approach to the physics of contacting surfaces. Tectonophysics 277, 29–40. https://doi.org/10.1016/S0040-1951(97)00076-0. URL:http://www.sciencedirect.com/science/article/pii/S0040195197000760. Earthquake Generation Processes: Environmental Aspects and Physical Modelling.
Yoshioka, N., Iwasa, K., 1996. The characteristic displacement in rate and state-dependent friction from a micromechanical point of view. Pure Appl. Geophys. 147, 433–453. https://doi.org/10.1007/BF00878837.
Yoshioka, N., Scholz, C.H., 1989. Elastic properties of contacting surfaces under normal and shear loads: 1. Theory. J. Geophys. Res.: Solid Earth 94, 17681–17690. https://doi.org/10.1029/JB094iB12p17681. URL:https://agupubs.onlinelibrary.wiley.co

m/doi/abs/10.1029/JB094iB12p17681, arXiv:https://agupubs.onlinelibrary.wiley.com/doi/pdf/10.1029/JB094iB12p17681.

Zhuo, Y.Q., Guo, Y., Chen, S., Ji, Y., Ma, J., 2018a. Laboratory Observations of Linkage of Preslip Zones Prior to Stick-Slip Instability. Entropy 20, 629.

Zhuo, Y.Q., Liu, P., Chen, S., Guo, Y., Ma, J., 2018b. Laboratory observations of tremor-like events generated during preslip. Geophys. Res. Lett. 45, 6926–6934. https://doi.org/10.1029/2018GL079201. URL:https://agupubs.onlinelibrary.wiley.com/doi/abs/10.1029/2018GL079201, arXiv:https://agupubs.onlinelibrary.wiley.com/doi/pdf/10.1029/2018GL079201.